"The Magnetized Interstellar Medium"
8–12 September 2003, Antalya, Turkey
Eds.: B. Uyanıker, W. Reich & R. Wielebinski

The Novelty of the Polarized Sky*

Bülent Uyanıker

Max-Planck-Institut für Radioastronomie, Auf dem Hügel 69, 53121 Bonn, Germany

Abstract. Observations of linear polarization in our Galaxy at centimeter wavelengths show unexpected objects and structural details. Little or no corresponding total-intensity emission from these polarization structures has been detected. These achievements in Galactic research reveal a new tool to probe the Galactic magnetic fields and the interstellar medium. It is the aim of this contribution to review some of these polarization structures and to report on recently detected features.

1 Introduction

Galactic radio polarization was discovered by Westerhout et al. (1962) and Wielebinski et al. (1962). Subsequently, a variety of surveys of the Galactic linear polarization were made: Berkhuijsen & Brouw (1963) at 408 MHz, Berkhuijsen et al. (1964) at 820 MHz, Spoelstra (1972) at 1.4 GHz. Brouw & Spoelstra (1976) collected all surveys made with the Dwingeloo 25-m telescope between 408 MHz and 1.411 GHz. These surveys are, however, largely undersampled. Moreover, they have coarse angular resolution ($36'$ at 1.4 GHz is the highest). After this pioneering work, the study of the polarization of diffuse Galactic emission was largely ignored, due to the difficulty of eliminating the instrumental polarization contribution to the detected signal. Nevertheless, the early, first-generation radio polarization surveys at low frequencies revealed substantial linear polarization from the diffuse Galactic emission, implying the general presence of ordered magnetic fields. Further measurements by Junkes et al. (1987) at 2.7 GHz and Wieringa et al. (1993) at 327 MHz triggered the second-generation surveys.

The second-generation, high-resolution surveys at 1.4 GHz, the Effelsberg Medium Latitude Survey (EMLS; Uyanıker et al. 1997, 1998, 1999, Reich et al., this volume), the Canadian Galactic Plane Survey (CGPS; Taylor et al. 2003, Uyanıker et al. 2003) and the Southern Galactic Plane Survey (SGPS; Dickey et al. 1999, Gaensler et al. 2001) show that at least some of this emission originates at distances up to a few kpc. Meanwhile, Duncan et al. (1999) made polarimetric measurements at 2.7 GHz. The current knowledge of the Galactic polarized emission is based on these two generations of surveys.

The highlights of the second-generation polarization research include the measurement of filamentary polarized structure on scales of a degree to a few arcminutes and the detection of dozens of depolarization structures (Uyanıker et al. 1997, 1999) at 1.4 GHz with the Effelsberg 100-m telescope, in the form of filaments, loops and arcs several degrees in size with no observable total-intensity counterpart. Gray et al. (1998) have also detected an interstellar Faraday rotation feature about $2°$ in size located in front of the prominent H II region W5, using the DRAO Synthesis Telescope at 1.4 GHz. This polarization structure also has no detectable total-intensity structure. Gaensler et al. (2001) studied diffuse polarized emission from the southern Galactic plane. Attempts to improve the Dwingeleo survey, in sensitivity, coverage and sampling, must also be mentioned here: the Villa Elisa southern survey by Testori et al. (this volume) and the Penticton survey by Wolleben et al. (this volume), both at 1.4 GHz and with a resolution of $36'$.

It is the aim of this contribution to review recently discovered objects, which enliven the polarization research. Most of these data come from the Effelsberg 100-m telescope and the DRAO Synthesis Telescope through the EMLS and CGPS. Other polarization features are discussed in the above-mentioned references (see also Haverkorn et al. 2000, 2003). The DRAO Synthesis Telescope receives

*Based on observations with the Effelsberg 100-m telescope operated by the Max-Planck-Institut für Radioastronomie (MPIfR), Bonn, Germany continuum signals in both hands of circular polarization in four separate bands of 1406.89, 1414.39, 1426.89, and 1434.39 MHz, each of width 7.5 MHz, on either side of the H I emission. This enables the determination of the rotation measure (RM). The EMLS was carried out at a frequency of 1400 MHz and partly in two frequency channels (Reich et al., this volume). The new Effelsberg system has eight bands centered at 1388, 1392, 1396, 1400, 1404, 1408, 1412, and 1416 MHz, each of width 4 MHz. The Effelsberg single-dish telescope is sensitive to large-scale structures not detectable in the CGPS, thus the RMs from both of these surveys will likely differ.

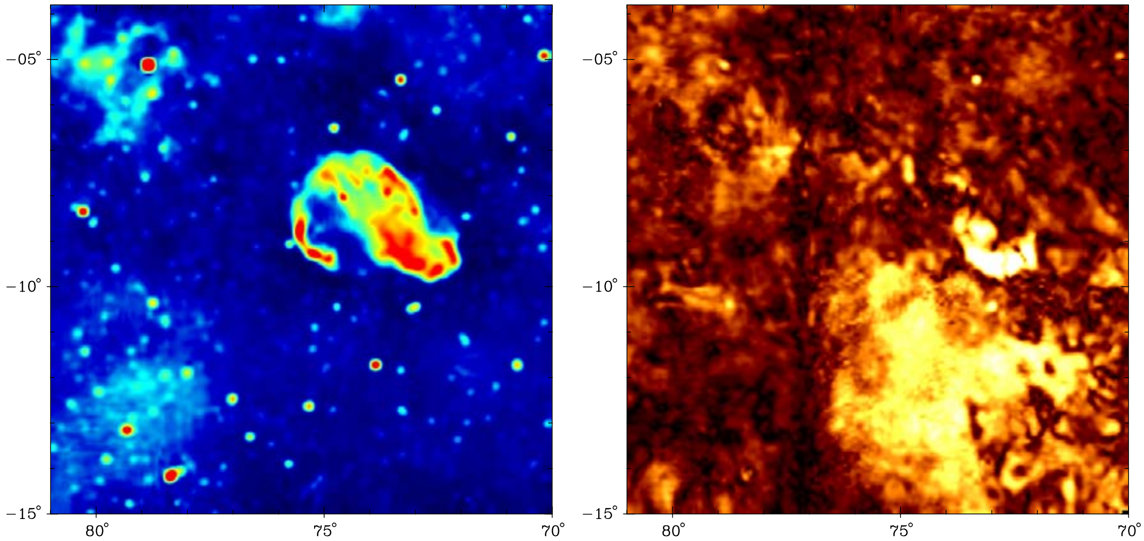

Fig. 1. The Cygnus patch in total intensity (left) and polarized intensity (right) taken from the EMLS (Uyanıker et al. 1997, 1999).

2 New features in the polarized sky

The second-generation surveys produced numerous interesting results with objects which were not known before. These surveys provided a new look in the polarized sky and changed our understanding of diffuse polarization enormously. In the following sections I give examples of new features in the polarized sky and present a new way of looking at previously known astronomical objects.

2.1 The Cygnus patch

One of the unexpected diffuse polarization data obtained during the EMLS were towards the Cygnus Loop supernova remnant (SNR). The total power (TP) and polarized intensity (PI) images of this area, at 1.4 GHz, are given in Fig. 1. The TP image displays a portion of the sky with spots of emission close to a SNR backgrounded with diffuse Galactic emission and extragalactic sources. The region is quite typical for regions close to the Galactic plane, except the SNR itself. However, the PI image encloses a remarkable $6\overset{\circ}{.}2 \times 5\overset{\circ}{.}6$ patch dominating the map and outshining the SNR's emission. The origin of this emission is still not known. But its existence hints that this object may be related to the irregularities in the magnetic field or thermal electron density in the line of sight. In this way this patchy emission could be interpreted as a result of Faraday modulation of the synchrotron background.

Later it became clear that this phenomenon, the anticorrelation of TP and PI, was ubiquitous. Among the many other examples of such structures in the EMLS, the region towards the Galactic anticenter (see Fig. 2) displays the strong contrast between the TP and PI images. Images from a synthesis telescope also show such an anticorrelation. Figure 3 includes a region towards lower longitudes obtained with the DRAO interferometer at the same frequency.

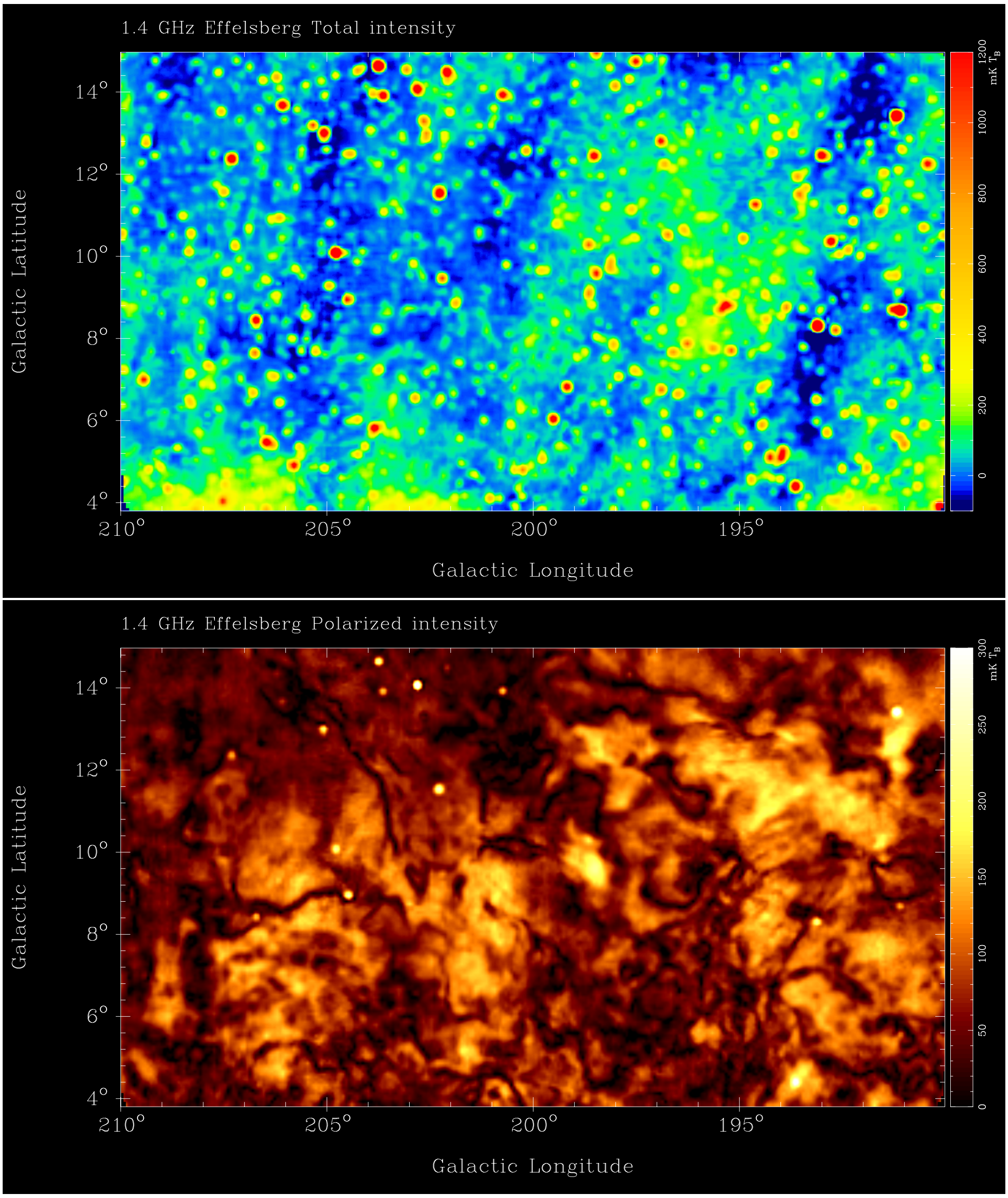

Fig. 2. The anticenter region in total intensity (top) and polarized intensity (bottom) taken from the EMLS (Uyanıker et al. 1999).

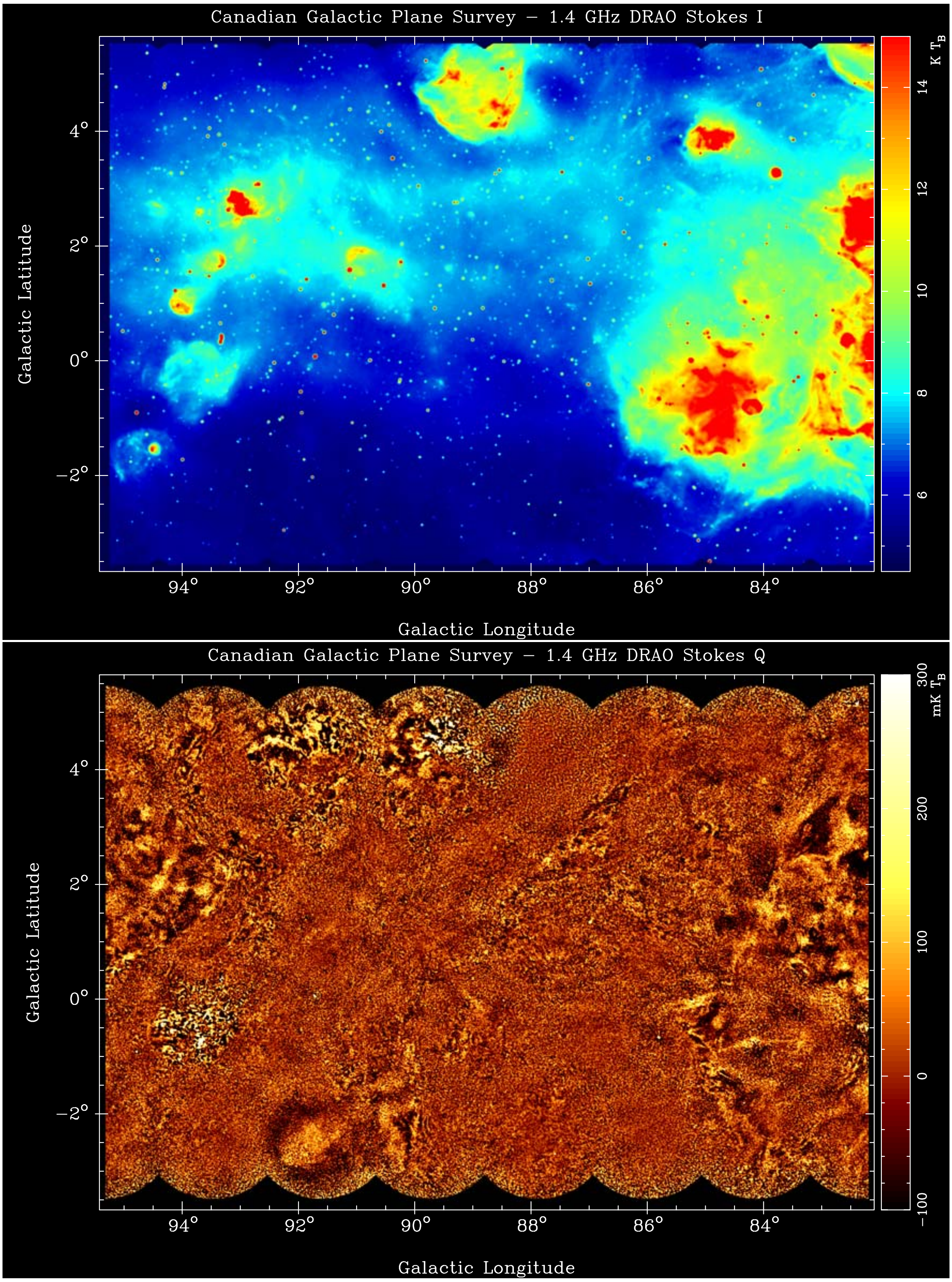

Fig. 3. The region towards the Cygnus arm in total intensity (top) and Stokes Q (bottom) taken from the CGPS (Uyanıker et al. 2003) with large-scale structures, in total intensity, added using the Effelsberg survey data by Reich et al. (1990) at the same frequency.

2.2 Canals and Faraday ghosts

The filamentary structures towards the anticenter region (Fig. 2) seem to be common in almost all polarization images at decimeter wavelengths. They resemble a network of randomly oriented structures where polarized intensity significantly diminished. The lack of associated total intensity, at first glance, implies that these structures are Faraday 'objects'. They can, of course, be formed by filamentary thermal plasma or appropriately aligned magnetic fields. The tool to discriminate between these two possibilities are multi-frequency observations. We expect these structures to vanish or change their shapes at higher frequencies if they are embodied by Faraday effects. In this case Faraday depolarization or beam depolarization are the possible origin of these structures. Otherwise, related objects causing such magnetic alignments must be sought.

The difficulty here, unfortunately, lies in the nonlinear relation between U and Q, which we use to calculate polarized intensity, PI=1/2 atan(U/Q). Missing flux in U and Q will reflect itself in the PI image drastically different than in the total intensity case. Missing large structures will considerably alter the U/Q ratio. An interferometer, for instance, assumes that the sum of the total observed flux within the field of view is zero. Therefore structures larger than provided by the shortest spacing will be lost. Accordingly, the resulting PI map not only lacks those large structures but also drafts a different composition between U and Q. In these measurements we customarily assume that U and Q are affected from the missing spacings in the same way. For some different alignment of U and Q this may not be the case at all.

The situation is similar in the single-antenna data. In contrast to the common expectation single-antenna measurements also suffer from missing flux, unless the measurements are absolutely calibrated. The required long integration time for absolute calibration does not allow large surveys. This is a trade between time and area covered. Hence, large-scale surveys have relative baselines, where the edges of the covered area are set to zero; meaning that structures larger than the area covered are not properly represented in the resultant map. In the EMLS, for instance, this corresponds to structures larger than about 10°, not severe when compared to interferometer data but still bearing the problem.

Therefore, structures attributed as Canals, see for example Fig. 2 or a recent paper by Shukurov & Berkhuijsen (2003), will most likely shift to a different position, weaken or disappear after the map is corrected for the missing flux. Probably the choice of the term 'ghosts' for these structures is also literally correct.

2.3 Depolarization effects

Beside the technical considerations mentioned above the most important effects reducing the fractional polarization are depolarization effects. If the rotation measure (RM) is high, the polarization angle changes across the bandwidth of the telescope, leading to averaging of the non-parallel vectors. In most of the modern surveys this upper limit of RM is about several 10^3 rad m^{-2}. This may have an immediate effect on some of the extragalactic objects with extraordinarily strong polarization characteristics. Therefore bandwidth depolarization does not impose serious limitations on the observed signal. Differential Faraday rotation (or depth depolarization) is one of the important effects shaping the observed polarization images, due to different rotation at different but superposed layers of Faraday-rotating material. The last one, beam depolarization, is an instrument- and wavelength-dependent effect and is responsible for averaging the polarization vectors if there are large RM gradients within the beam of the telescope. Beam depolarization further gives rise to Faraday dispersion, and hence depolarization, if there are many small-scale turbulent structures within the beam. Another important issue needs to be emphasized here: the calculation of RM may be misleading if the rotation is not linearly proportional to λ^2.

2.4 Polarization horizon

The existence of depolarization alone hints that there exists a maximum distance which can be probed at a particular wavelength with a given telescope. This maximum distance further depends on the portion of the sky observed (i.e. electron density in the line of sight) and on the strength of the magnetic field in that direction. This maximum distance is called the “polarization horizon” (Uyanıker et al. 2003) and is determined to be about 2 kpc towards the Cygnus arm ($\ell \sim 70°$). It seems that the horizon has also a similar value up to longitudes $\ell \sim 115°$. However, towards the anticenter, due to the existence of relatively less ionizing material, the horizon should extend further and in this direction ‘looking’ deeper into the Galaxy should be possible. It is obvious that the polarization horizon is not single-valued and varies with the wavelength of the observation and physical parameters along the line of sight. This, however, infers a strong relationship between the detectability of the polarized emission and the distance from which it originates.

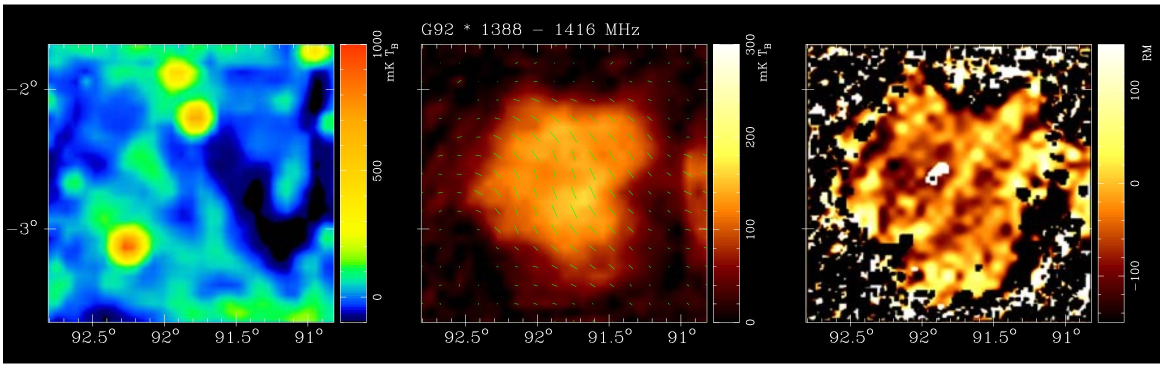

Fig. 4. TP, PI (with E-vectors) and RM images of the G91.8−2.5 lens from the 8-channel Effelsberg observations.

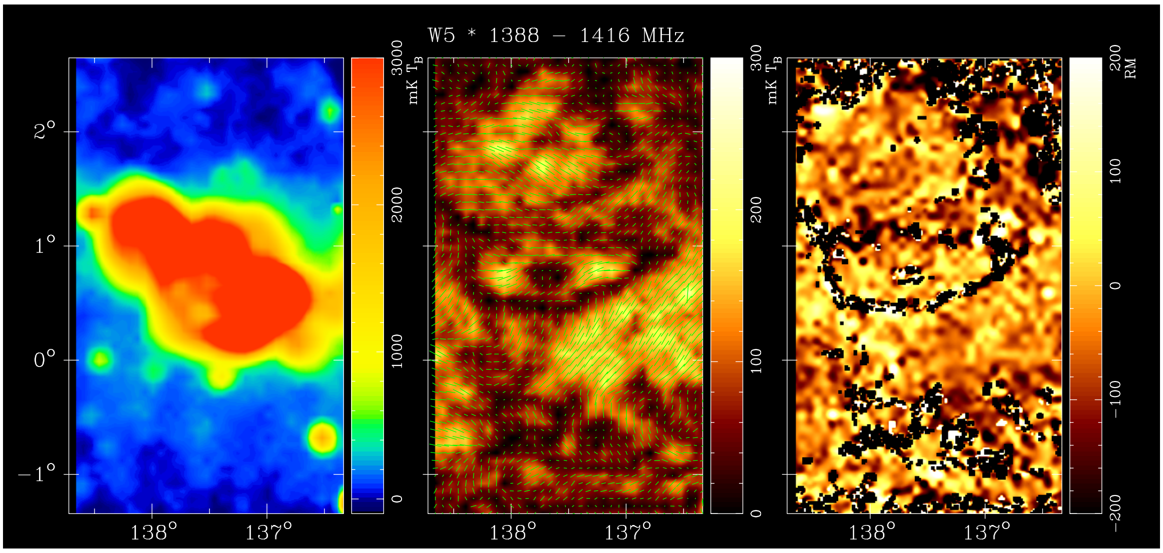

Fig. 5. TP, PI (with E-vectors) and RM images of the W5-lens from the 8-channel Effelsberg observations.

2.5 The polarized lenses (G91.8−2.5 and G137.6+1.1)

Another surprising result was the detection of a “polarized lens” structure (G91.8−2.5; Uyanıker & Landecker, 2002). This Faraday-rotation structure (see Fig. 4) detected through polarimetric imaging at 1.4 GHz has an extent of 2°, within which the polarization angle varies smoothly over a range of $\sim 100°$. The region is in sharp contrast to its surroundings, where low-level chaotic polarization structures are seen. The absence of a counterpart, in either optical or total intensity, establishes a lower limit to its distance. An upper limit can be determined by the strong beam depolarization.

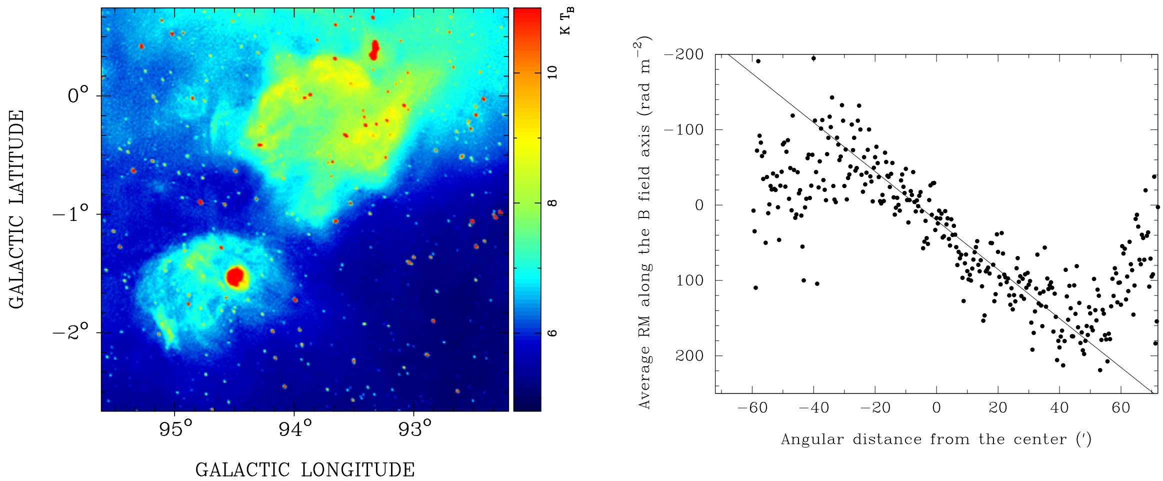

Fig. 6. Left: Total intensity image of CTB104A ($\ell \sim 93\overset{\circ}{.}7$, $b \sim -0\overset{\circ}{.}3$), as observed with the DRAO Synthesis Telescope at 1.4 GHz. The structure at the lower left is the H II region S 124. Right: projection of RM values onto the magnetic axis of the remnant. This RM gradient, increasing with longitude, indicates a magnetic field orientation in the opposite direction as suggested by the pulsar RM data (Uyanıker et al. 2002).

Uyanıker & Landecker (2002) give a distance of 350±50 pc for this object, which in turn implies a linear size of 10 pc, an enhancement of electron density of 1.7 cm^{-3} and a mass of ionized gas of $M \simeq 23\,\mathrm{M}_{\odot}$. The new map with the Effelsberg 8-channel system (see Fig. 4) confirms the results of the interferometer data, giving an average rotation measure of RM $= -27$ rad m^{-2} across the polarized lens. The importance of this feature is that it might belong to a new class of objects. There are some similarities between this object and the structure towards W5 detected earlier (G137.6+1.1; Gray et al. 1998). Such objects might be quite common in the interstellar medium.

The almost perfectly elliptical W5-lens, according to Gray et al. (1998), was a result of Faraday modulation as in the Cygnus patch or in the anticenter filaments. They have placed this object between us and the large H II region W5 with a systematic RM gradient across the object of ΔRM $\sim$ 110 rad m^{-2}. The Effelsberg 8-channel data on the other hand give RM values between ±100 rad m^{-2} with an average value of 2 rad m^{-2}. The crucial point here, however, is that the RM values within the lens and outside the lens are similar (see Fig. 5). Such a fortuitous alignment is unlikely. Therefore, the properties of the interstellar medium towards the lens are more likely to have similar properties as the surroundings. If the lens consists of ionized gas causing the RM variation, its density would be so high that would not be missed in the total-intensity emission. With these properties the W5-lens looks like a ring which can only be traced in polarized emission. A detailed investigation of this lens, combined with data at other frequencies, will provide more information on this class of objects.

2.6 Probing the Galactic magnetic field via SNRs

Beside the diffuse polarized emission in the Milky Way, the effects of the large-scale magnetic field and its interaction with the interstellar material can be studied towards SNRs (see Fürst & Reich, this volume). In due course of their evolution SNRs bend and stretch the surrounding magnetic field with their strong shocks, according to the van der Laan model–punching magnetic holes in the uniform background magnetic field. Therefore, any study of diffuse magnetic fields in the Galaxy ignoring SNRs is incomplete.

The investigation of polarized emission, in particular the RM data towards SNRs, is a powerful method to reveal the interaction of the Galactic magnetic field with the SNRs. Small-scale polarization and RM structures are turbulent in nature, but towards SNRs there are well-ordered RM gradients. The first clear example of such an RM gradient has recently been studied by Uyanıker et al. (2002) towards the mature supernova remnant CTB104A, at a distance of 1.5 kpc. The observed gradient, extending from southeast to northwest (see Fig. 6) does not agree with the direction of the global

Galactic magnetic field (see Han, this volume), but does agree with a large-scale RM anomaly inferred from rotation measure data by Clegg et al. (1992). Clearly, the observed morphology of CTB104A is consistent with expansion in a uniform magnetic field, and this is supported by the observed RM distribution. The shock of the explosion compresses and deforms the ambient magnetic field and thus the remnant outlines the signature of the local magnetic field. The direction of the RM gradient defines the axis of the magnetic field around the remnant, making 60° with the Galactic plane.

The current method to determine the direction of the magnetic field in the Galaxy is the use of pulsar rotation measures (see Han et al. 1999, Han, this volume), because they are relatively easy to measure and distances of pulsars, based on their dispersion measure, are known. According to these data, the direction of the ambient magnetic field is pointing away from us and directed towards lower longitudes. However, the observed RM gradient decreases in the opposite direction, namely the RM is increasing with longitude. This implies an ambient magnetic field direction opposite to the overall Galactic magnetic field. Thus the orientation of the magnetic field in this region is not parallel to the Galactic plane, nor in agreement with the "large-scale" Galactic field, but is consistent with the RM anomaly observed by Clegg et al. (1992).

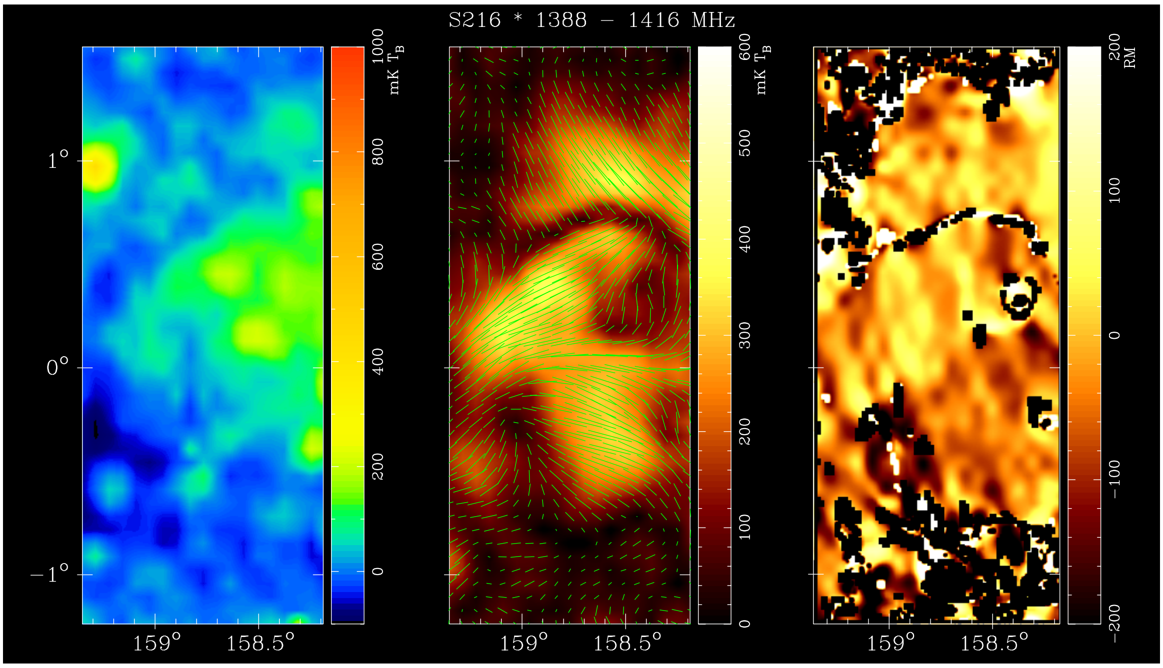

Fig. 7. TP, PI (with E-vectors) and RM images of S216 from the 8-channel Effelsberg observations.

2.7 S216: A planetary nebula acting as Faraday screen

Polarized structures of Galactic radio emission at centimeter wavelengths, showing no or little correlation with the total radio emission, are attributed to rapid changes in Faraday rotation through a foreground magneto-ionic medium (MIM) – the so-called "Faraday screen". The origin and distances of these polarization structures, however, remained unknown. We observe considerable linearly polarized emission towards the planetary nebula S216. However, there is distinct but weak total-intensity emission (see Fig. 7), resulting in an unphysically large fractional polarization in excess of 100 %. Apparent excess percentage polarization is a definitive signature of a Faraday screen. Such a screen can be detected only in polarization because any relative irregularity in Stokes U and Q, carrying directional information of the magnetic field, is picked up by the polarimeter, while large-scale information remains undetected. Here I report the discovery of a Faraday screen feature associated with a known astronomical object – the planetary nebula (PN) S216 (Uyanıker, in preparation).

This result is surprising because planetary nebulae are known to be unpolarized at radio wavelengths and they are similar to H II regions in terms of their thermal emission. However, the highly ionized ejected atmosphere of the progenitor star of S216 apparently prepared conditions similar to those a Faraday screen is made of.

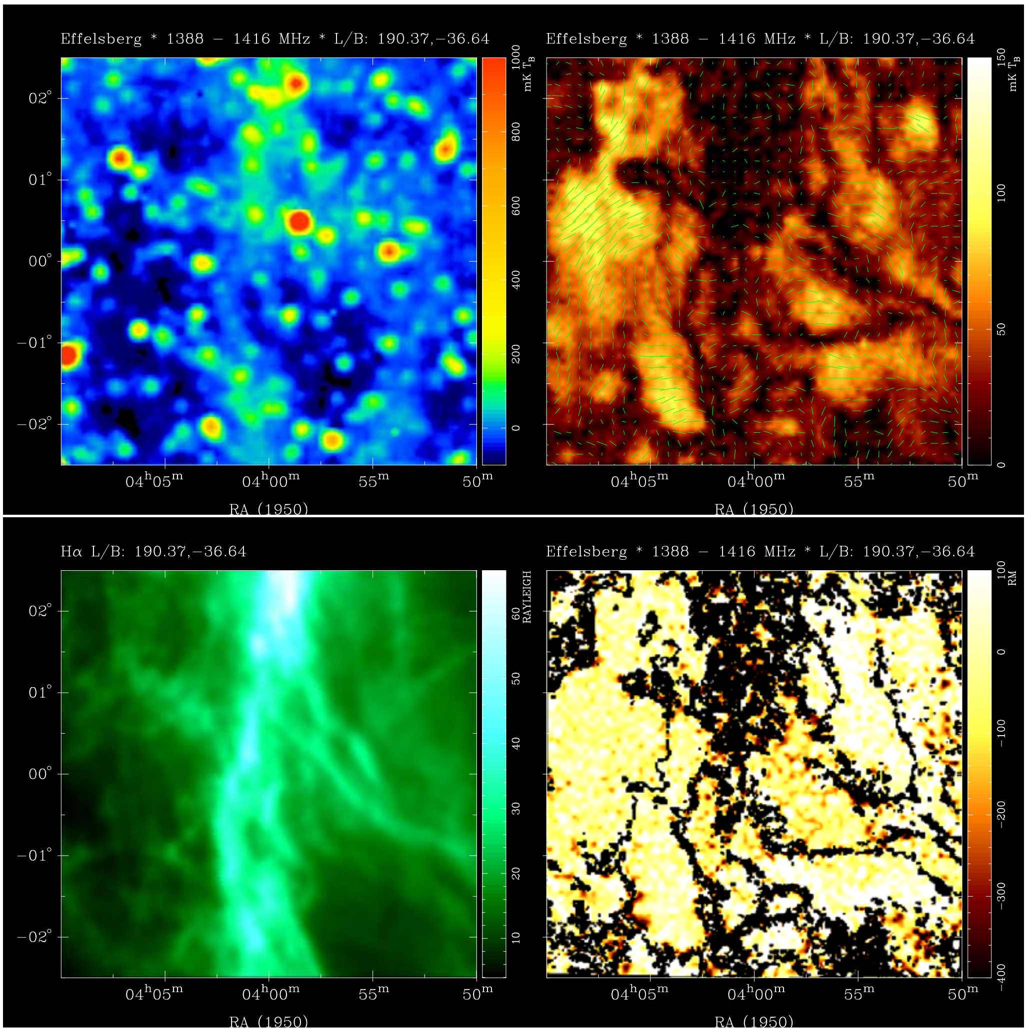

Fig. 8. Effelsberg 8-channel data towards the MBM 18 molecular cloud at 1.4 GHz. *Top:* Combined total-intensity (left) and polarized-intensity images between 1.388 and 1.416 GHz. Overlaid bars denote the electric field vectors. *Bottom:* Hα (left) image and the rotation-measure map of the same region.

2.8 The MBM 18 molecular cloud

Another example showing how an Hα filament positionally coinciding with a molecular cloud is acting as a Faraday screen comes from the Effelsberg 8-channel test measurements at 1.4 GHz, exhibiting the power of closely separated multi-frequency observations in the polarization domain.

MBM 18 ($\ell = 190.^{\circ}37$, $b = -36.^{\circ}6$; also known as LDN 1569) is at a distance of ~130 pc and located where the Orion-Eridanus Bubble and the Local Hot Bubble collide. Figure 8 shows the combined 8-channel maps of total intensity, polarized intensity and the Hα image towards MBM 18 in a region of $5^{\circ} \times 5^{\circ}$, together with the derived rotation-measure map. The value of these observations, beyond detecting a Faraday screen from a molecular cloud, must be stressed here: there exists no rotation measure information at these high latitudes comparable to the sensitivity of the Effelsberg telescope (about 15 mK in total intensity and 8 mK in the U and Q channels), coherently covering large areas and eight successive frequencies with a resolution of 9′. These data do not simply surpass any existing diffuse polarization data but also provide rotation-measure information, which is crucial in interpreting and analyzing such structures.

The results of the test measurements with the Effelsberg 8-channel system will be given elsewhere (Uyanıker et al., in preparation).

3 Conclusions

Recent achievements in Galactic research reveal a new tool for the investigation of Galactic magnetic fields and the interstellar medium. Observations of linear polarization in our Galaxy at centimeter wavelengths show unexpected structural details. Little or no corresponding total-intensity emission from these polarization structures has been detected. High-sensitivity and high-resolution measurements of Stokes U and Q at a range of frequencies are needed to measure RM and to allow us to interpret this phenomenon. High angular resolution, achievable only with aperture synthesis telescopes, is needed to measure the fine details. However, such telescopes miss the diffuse emission. High-sensitivity data from single-antenna telescopes are essential to understand the phenomenon on large scales. Supernova remnants, which both influence and are influenced by the Galactic fields, also need a combination of interferometer and single-dish studies to understand their magnetic field geometries.

In spite of the observational difficulties recent results open a new window to the interstellar medium by the detection of previously unexpected objects. Thus the strength of polarization measurements to apprehend the nature of the magnetic fields became more appreciable. With future observations and continuing effort we expect to improve our perception towards understanding magnetic fields.

Acknowledgments

The Effelsberg 8-channel polarization mapping project is carried out with contributions from W. Reich, P. Reich, E. Fürst & R. Wielebinski from the MPIfR continuum group.

References

Berkhuijsen E.M. & Brouw W.N. (1963) *Bull. Astr. Inst. Neth.* **17**, 185.
Berkhuijsen E.M., Brouw W.N., Muller C.A. & Tinbergen J. (1964) *Bull. Astr. Inst. Neth.* **17**, 465.
Brouw W.N. & Spoelstra T.A.Th. (1976) *Astron. Astrophys. Suppl.* **26**, 129.
Clegg A.W., Cordes, J.M., Simonetti, J.H. & Kulkarni, S.R. (1992) *Astrophys. J.* **386**, 143.
Dickey J.M., McClure-Griffiths N., Gaensler, B. et al. (1999) in *New Perspectives on the Interstellar Medium*, eds. A.R. Taylor, T.L. Landecker & G. Joncas, ASP Conf. Ser. **168**, p. 27.
Duncan A.R., Haynes R.F., Jones K.L & Stewart R.T. (1997) *Mon. Not. R. Astron. Soc.* **291**, 279.
Gaensler B.M., Dickey, J.M., McClure-Griffiths, N.M. et al. (2001) *Astrophys. J.* **549**, 959.
Gray A., Landecker T.L., Dewdney P.E. & Taylor A.R. (1998) *Nature* **393**, 660.
Haverkorn M., Katgert P. & de Bruyn A.G. (2000) *Astron. Astrophys.* **356**, 13.
Haverkorn M., Katgert P. & de Bruyn A.G. (2003) *Astron. Astrophys.* **403**, 1031.
Junkes N., Fürst E. & Reich W. (1987) *Astron. Astrophys. Suppl.* **69**, 451.
Shukurov A. & Berkhuijsen E.M. (2003) *Mon. Not. R. Astron. Soc.* **342**, 496.
Spoelstra T.A.Th. (1972) *Astron. Astrophys. Suppl.* **21**, 61.
Taylor A.R., Dougherty S.M., Gibson S.J. et al. (2003) *Astron. J.* **125**, 3145.
Uyanıker B., Fürst E., Reich W., Reich P. & Wielebinski R. (1997) in *The Local Bubble and Beyond*, IAU Coll. 166, eds. D. Breitschwerdt et al., Springer Lecture Notes in Physics **506**, p. 239.
Uyanıker B., Fürst E., Reich W., Reich P. & Wielebinski R. (1998) *Astron. Astrophys. Suppl.* **132**, 401.
Uyanıker B., Fürst E., Reich W., Reich P. & Wielebinski R. (1999) *Astron. Astrophys. Suppl.* **138**, 31.
Uyanıker B., Kothes R. & Brunt C.M. (2002) *Astrophys. J.* **565**, 1022.
Uyanıker B., Landecker T.L., Kothes R. & Gray A.D (2003) *Astrophys. J.* **585**, 785.
Westerhout G., Seeger Ch.L., Brouw W.N. & Tinbergen J. (1962) *Bull. Astr. Inst. Neth.* **16**, 187.
Wielebinski R., Shakeshaft J.R. & Pauliny-Toth I.I.K. (1962) *Observatory* **82**, 158.
Wieringa M.H., de Bruyn A.G., Jansen D., Brouw W.N. & Katgert P. (1993) *Astron. Astrophys.* **268**, 215.

"The Magnetized Interstellar Medium"
8–12 September 2003, Antalya, Turkey
Eds.: B. Uyanıker, W. Reich & R. Wielebinski

Unraveling the Structure in the ISM Through Radio Polarimetry

M. Haverkorn[1,2], P. Katgert[2], A. G. de Bruyn[3,4] and F. Heitsch[5,6]

[1] Harvard-Smithsonian Center for Astrophysics, 60 Garden Street MS-67, Cambridge MA 02138, USA
[2] Leiden Observatory, P.O.Box 9513, 2300 RA Leiden, the Netherlands
[3] ASTRON, P.O.Box 2, 7990 AA Dwingeloo, the Netherlands
[4] Kapteyn Institute, P.O.Box 800, 9700 AV Groningen, the Netherlands
[5] Max-Planck-Institut für Astronomie, Königstuhl 17, 69117 Heidelberg, Germany
[6] University of Wisconsin-Madison, 475 N Charter St, Madison, WI 53706, USA

Abstract. We present two models of the Galactic warm interstellar gas to study depolarization and derive properties of the interstellar medium (ISM). First, a single-cell-size model of the ISM including magnetic fields and thermal and relativistic electrons is used to derive the magnetic field strength and typical scale of structure in the ISM. The polarized radiation in the model is compared to observations of the polarized synchrotron background at 350 MHz, taken with the Westerbork Synthesis Radio Telescope (WSRT). The modeling yields a random magnetic field component $B_{ran} \approx 1 - 3$ μG, a regular magnetic field component $B_{reg} \approx 2 - 4$ μG directed almost perpendicular to the line of sight, and a typical scale of the structure $d \approx 15$ pc. A three-dimensional magnetohydrodynamical model of a Faraday screen is used to estimate the effect of beam depolarization on diffuse polarization observations. It suggests that sharp gradients in RM are a common feature in the warm ISM, and that the depolarization canals in the WSRT observations are most likely caused by beam depolarization. The additional error in RM in these observations introduced by beam depolarization is estimated to be ∼20%.

1 Introduction

The linearly polarized component of the ubiquitous diffuse Galactic synchrotron emission undergoes Faraday rotation and depolarization while propagating through the interstellar medium (ISM). When polarized radiation propagates through a magneto-ionized medium, the polarization angle ϕ is rotated according to $\phi = \phi_0 + RM\lambda^2$, where ϕ_0 is the intrinsic polarization angle and RM is the rotation measure. The rotation measure depends on the parallel component of the magnetic field $B_\parallel$, the thermal electron density n_e and the path length ds as RM [rad m^{-2}] $= 0.81 \int B_\parallel[\mu\text{G}]\, n_e[\text{cm}^{-3}]\, ds[\text{pc}]$. Depolarization can be due to Faraday rotation in a synchrotron emitting medium and/or due to structure in the magnetic field. In our observations, depolarization occurs along the line of sight (depth depolarization) and within the beam width (beam depolarization), see e.g. Burn (1966), Gardner and Whiteoak (1966), Sokoloff et al. (1998), or Haverkorn et al. (2003a).

The observations are briefly discussed in Sect. 2. In Sect. 3, we present the first effort using the diffuse synchrotron background to derive the properties of the small-scale magnetic field. In Sect. 4, we discuss a magnetohydrodynamical model of the Faraday-rotating medium used to investigate the origin of "depolarization canals", i.e. long and narrow structures of complete depolarization present in many observations.

2 The observations

With the Westerbork Synthesis Radio Telescope (WSRT), we performed polarimetric observations at five frequencies around 350 MHz in two fields of view in the constellations Auriga and Horologium at Galactic latitudes $b = 16^\circ$ and 8° respectively, in the second Galactic quadrant, with a resolution of $4'$ (Haverkorn et al. 2003b, 2003c). The linearly polarized intensity $P = \sqrt{Q^2 + U^2}$ in the two fields is given in Fig. 1 in grey scale, with a maximum of ~ 13 K in white. From the polarization angles $\phi = 0.5 \arctan(U/Q)$ at five frequencies the rotation measure $RM = \phi_0 + RM\lambda^2$ was derived, which is shown as circles in Fig. 1. Only "reliably determined" RMs are used and displayed, i.e. RMs for which the reduced χ^2 of the linear $\phi(\lambda^2)$-relation $\chi_r^2 < 2$ and which have a signal-to-noise larger than five. A best-fit gradient of RM in the Auriga field is subtracted.

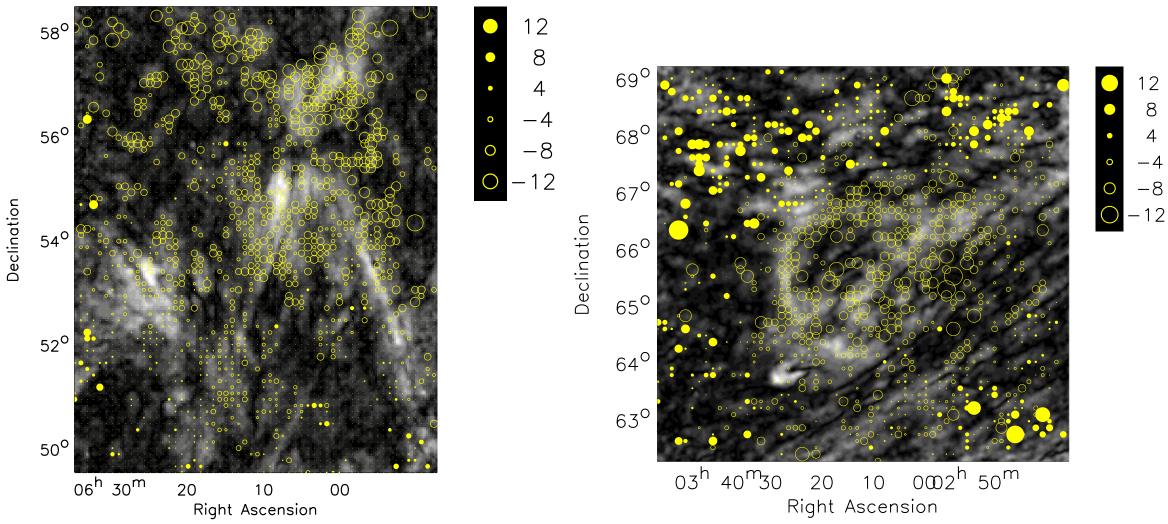

Fig. 1. Polarized intensity in grey scale in Auriga (left) and Horologium (right), overlaid with RM in yellow circles. Filled (Open) circles denote positive (negative) RMs, and the size of a circle scales with the magnitude of RM.

3 A model of the magneto-ionized medium

We constructed a model of the magneto-ionized thin disk of the Galaxy, including synchrotron emission and Faraday rotation. From comparison of the model properties with the observations, we can estimate the strengths of the regular and random components of the Galactic magnetic field, and the typical scale of the structure (for details see Haverkorn et al. (2003d)).

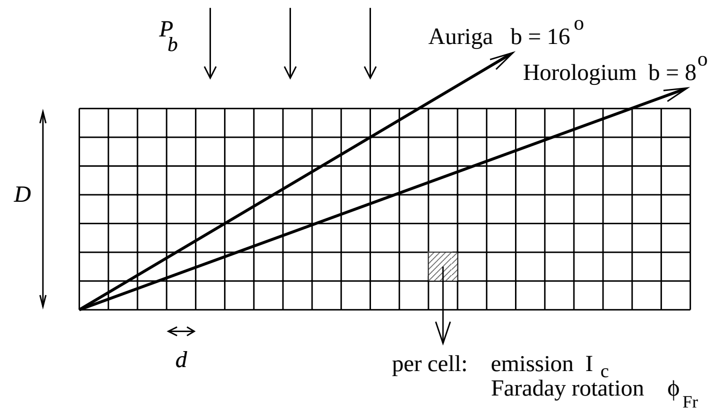

Fig. 2. Model of the magneto-ionized thin disk, consisting of cells with size d in a layer of thickness D, irradiated by a polarized background P_b. Each cell emits synchrotron radiation I_c, and a selection of cells Faraday rotates. Polarization properties along two lines of sight are compared to observations in the Auriga and Horologium field.

The model is outlined in Fig. 2. It consists of cells of size d in a layer of thickness D, which coincides with the thin disk. We attribute a constant regular magnetic field to each cell, and a random magnetic field component with a constant strength but a random direction per cell. Synchrotron radiation I_c is emitted in each cell, but the thermal electron density is only non-zero in a randomly chosen fraction f of the cells to mimic the filling factor of the warm ionized gas. Therefore, cells without thermal electrons denote the hot and cold gas, which is assumed to contribute negligibly to the Faraday rotation.

The thin disk is irradiated from above with a constant polarized intensity $P_b = 0.7\eta_b I_b$, where I_b is the total synchrotron intensity of the background. η_b is a factor denoting the depolarization of the background ($0 < \eta_b < 1$), as the background can be partially uniformly depolarized by differential Faraday rotation along the line of sight. The factor 0.7 indicates the intrinsic degree of polarization of synchrotron radiation $p = P/I \approx 0.7$ (Burn 1966). So the background radiation, combined with the radiation from the cells, propagates through the model, which yields a value for Q and U. Modeling five frequencies, we can compute a rotation measure for a line of sight. We obtain a statistical ensemble by redrawing the same line of sight many times for different directions of the random magnetic field and different cells containing thermal electron density. The resulting distributions of Stokes Q and U and of RM are compared to the observed distributions shown in Fig. 3.

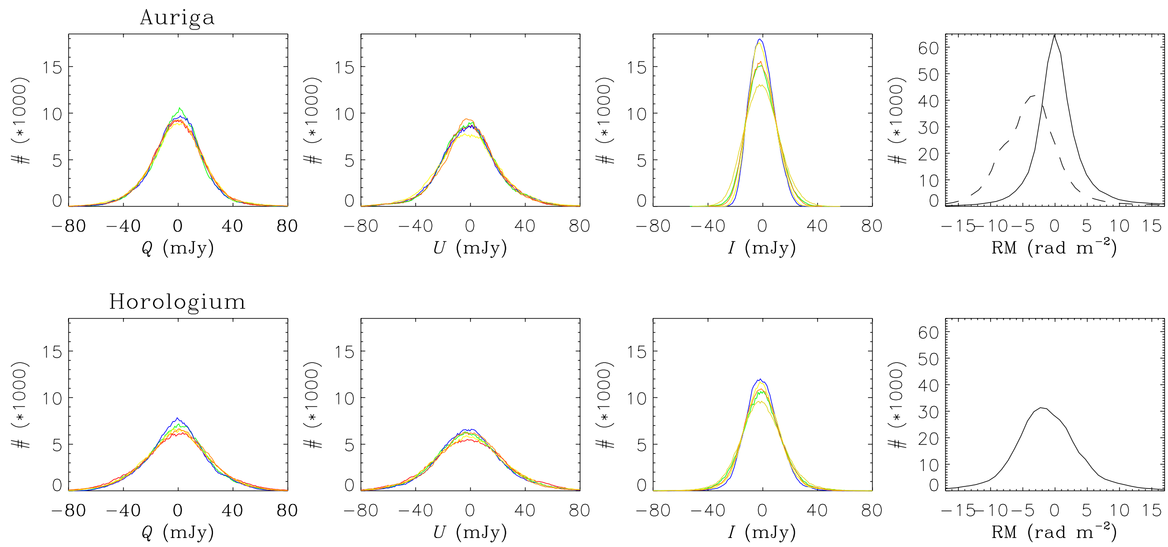

Fig. 3. Histograms of (from left to right) Q, U and I for 5 frequencies overplotted, and RM, for Auriga (top) and Horologium (bottom). Red, green, blue, yellow and orange lines denote the frequencies 341, 349, 355, 360, and 375 MHz, respectively. Data of Q, U and I are 5 times oversampled, and only reliably determined RMs are included. In the solid line histogram of RM in the Auriga region, a best-fit RM gradient over the region is subtracted; the dashed line gives the histogram of the observed RM including the gradient.

It is unknown how the random magnetic field in the warm magneto-ionized gas relates to the random magnetic field in the hot and cold gas. We therefore considered two models A and B which have different random magnetic fields in the hot and cold gas, i.e. in those cells that do not contain thermal electrons. In model A, the properties of both the random and the regular component of the magnetic field are identical in all cells. In model B, the random component of the magnetic field is only non-zero in the warm ISM.

The results are shown in Fig. 4 for models A (left) and B (right) as a function of cell size. From top to bottom, the figure shows model estimates for the regular magnetic field parallel to the line of sight $B_{reg,\|}$, the random magnetic field B_{ran}, the perpendicular regular magnetic field $B_{reg,\perp}$, the polarized intensity of the background P_b, the depolarization factor η_b, the ratio of random to regular magnetic field B_{ran}/B_{reg} and the total intensity emitted only in the thin disk $I_{0,thin}$. The red lines and regions denote lines of sight towards the Auriga field, the yellow lines and regions those towards Horologium.

The most important conclusions are:

- In both fields the perpendicular component of the regular magnetic field is much larger than the parallel component, indicating that the regular magnetic field is directed almost in the plane of

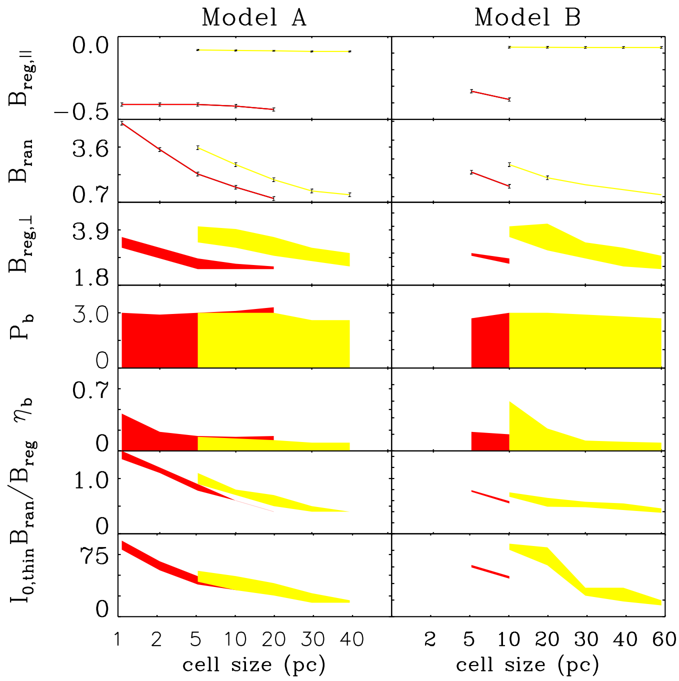

Fig. 4. Values for the random and regular magnetic field components $B_{reg,\|}$, B_{ran}, and $B_{reg,\perp}$, for the polarized intensity of the background P_b, the depolarization factor η_b, the ratio of random to regular magnetic field B_{ran}/B_{reg} and the total intensity emitted in the thin disk $I_{0,thin}$ in the Auriga (red) and Horologium (yellow) regions.

the sky. This is what is expected for these directions of observation for a regular magnetic field aligned along the spiral arms;

- The typical scale of structure in RM is $d = 15 \pm 10$ pc;
- The random magnetic field is about $B_{ran} \approx 3$ μG. The ratio of random to regular magnetic fields B_{ran}/B_{reg} is generally slightly below 1, smaller than most other determinations (Beck et al. 1996; Heiles 1996). This can have several reasons: first, structure in the magnetic field on scales larger than the size of the observed fields ($\sim 7°$) is interpreted as regular magnetic field in the models. Furthermore, our lines of sight are mostly located in interarm regions, where B_{ran}/B_{reg} is believed to be lower than in the spiral arms (e.g. Beck 2001). Finally, the two fields were selected for their conspicuous large-scale structure in polarization, which indicates a more regular magnetic field than average.

4 Steep gradients of RM in the ISM

A particularly striking feature in many diffuse polarized intensity maps is the presence of "depolarization canals", which are long and narrow (one beam wide) structures of complete depolarization (e.g. Duncan et al. 1997; Uyanıker et al. 1999; Gaensler et al. 2001; Haverkorn et al. 2003b,c). Across these canals, the polarization angle changes by 90° (Haverkorn et al. 2000). Both beam and depth depolarization can cause complete depolarization accompanied by a change in polarization angle of 90°. We used a MHD model of a Faraday screen which only contains beam depolarization but no depth depolarization to study beam depolarization as a cause for canals.

A sharp 90° change in polarization angle ϕ within one beam completely depolarizes the beam. If such a sharp gradient in ϕ extends over several beams perpendicular to the direction of the gradient, this causes depolarization in a one-beam wide canal. A change in $\phi = \phi_0 + RM\lambda^2$ can be caused by either a change in RM or in ϕ_0. The properties of the observed depolarization canals can distinguish between these two scenarios: if the canals are stable in position as well as in depth with frequency, $\Delta\phi$ is caused by $\Delta\phi_0$. On the other hand, if the canals do not shift position with frequency, but do vary in depth, they are caused by ΔRM. The observations show a change in depth of the canals without accompanying change in position, indicating that the canals are caused by a steep ΔRM within the beam. Therefore, beam depolarization provides a natural explanation for the fact that the canals are only one beam wide, and do not shift position with frequency, and is the most likely process to produce the canals in the observations discussed above (Haverkorn et al. 2003a). However, it requires an ISM in which sharp and narrow gradients in RM are a common feature.

We constructed a 3-dimensional magnetohydrodynamical (MHD) model using the Eulerian MHD code ZEUS-3D (Stone and Norman 1992a,b; Haverkorn and Heitsch 2004). Turbulence in the model volume is driven on the largest scales, and turbulent energy cascades down to smaller scales until the diffusion scale. The turbulent medium was irradiated from behind with a constant 100% polarized background radiation, which was Faraday-rotated while propagating through the model. Subsequently, the Stokes parameters Q and U were smoothed with a Gaussian of width σ to simulate a telescope beam. The polarized intensity passing through the model volume is constant, because the medium only rotates ϕ. However, the smoothing of Q and U effectively introduces beam depolarization in the radiation, and the "smoothed" polarized intensity $P_s = \sqrt{Q_s^2 + U_s^2}$ (with Q_s and U_s the smoothed Q and U) does show small-scale structure.

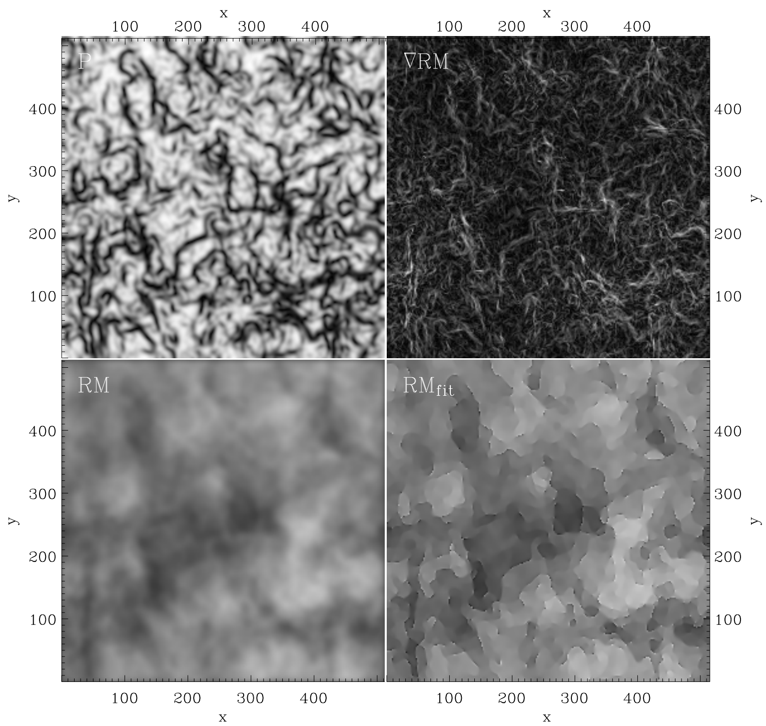

Fig. 5. Results from the 3-dimensional MHD model volume of a Faraday screen. Polarized radiation, propagating through the medium, was smoothed with a Gaussian of width σ to simulate a finite telescope beam. Top left: polarized intensity. Bottom left: original rotation measure in the modeled volume. Top right: gradient in the original RM. Bottom right: RM as computed from the smoothed values of Stokes Q and U.

In Fig. 5, the top left display shows the smoothed polarized intensity P_s, where white is high intensity. Depolarization canals are abundant. The bottom left map shows the RM of the medium, where $|\mathrm{RM}| \lesssim 15$ rad m^{-2}. There is no direct correlation visible between RM and P_s. However, the gradient in RM, shown in the top right map of Fig. 5, is strongly correlated to P_s. At those positions where a steep gradient in the RM is present, a depolarization canal forms, suggesting that depolarization canals caused by sharp RM gradients are a common feature (Haverkorn and Heitsch 2004). The role played by magnetic field and/or electron density in causing the sharp gradients in RM will be discussed in a forthcoming paper.

We compare the original RM in the modeled medium to RM values computed from the smoothed Q and U to estimate the influence of beam depolarization on RM determination. RM_s is computed from the smoothed polarization angle $\phi_s = 0.5 \arctan(U_s/Q_s)$. The lower right map in Fig. 5 shows the RM computed from the smoothed Q and U values, RM_s. The general features of the structure in RM are preserved, although in detail the RM values from the smoothed data differ from the original RM. RM_s also exhibits anomalous values in elongated structures on sub-beam scales, which are also observed (Haverkorn and Heitsch 2004). These anomalous RMs coincide with depolarization canals, in which the signal-to-noise is so low that reliable determination of RM is not possible. Furthermore, for observables as in the observations discussed above, the computed RM in general does not deviate from the original RM by more than 20%.

5 Conclusions

Modeling of the diffuse synchrotron background provides information on the Galactic magnetic field strength and structure. We compared results from a simple single-cell-size model of the warm magneto-ionized interstellar gas, including Faraday rotation and depth depolarization, to observations of the synchrotron background in two fields in the second Galactic quadrant. The model yields a random Galactic magnetic field of $1 - 3$ μG, and a somewhat higher regular magnetic field, directed almost in the plane of sky, with a typical scale of structure of $d = 15 \pm 10$ pc.

A magnetohydrodynamical model of a Faraday screen irradiated with polarized emission was used to gauge the amount of beam depolarization. Sharp gradients in RM on sub-beam scales, which cause depolarization in long narrow depolarization canals, appear to be abundant in the modeled ISM. For the observations discussed above, an additional error in the RM of $\sim$ 20% is introduced by beam depolarization.

Acknowledgments

Computations were performed on the SGI Origin 2000 of the National Center for Supercomputing Applications (NCSA) at Urbana-Champain. ZEUS-MP was used by courtesy of the LCA (Laboratory of Computational Astrophysics, NCSA). We are grateful to P. S. Li and M. L. Norman for making the 512^3 available. The Westerbork Synthesis Radio Telescope is operated by the Netherlands Foundation for Research in Astronomy (ASTRON) with financial support from the Netherlands Organization for Scientific Research (NWO). M.H. is supported by NWO grant 614-21-006. F.H. is supported by a Feodor-Lynen fellowship of the Alexander-von-Humboldt Foundation and by NSF grant AST-0098701.

References

Beck R. (2001) *Space Science Rev.* **99**, 243.
Beck R., Brandenburg A., Moss D., Shukurov A., Sokoloff D. (1996) *Annnu. Rev. Astron. Astrophys.* **34**, 155.
Burn B.J. (1966) *Mon. Not. R. Astron. Soc.* **133**, 67.
Duncan A.R., Haynes R.F., Jones K.L., Stewart R.T. (1997) *Mon. Not. R. Astron. Soc.* **291**, 279.
Gaensler B.M., Dickey J.M., McClure-Griffiths N.M., Green A.J., Wieringa M.H., Haynes R.F. (2001) *Astrophys. J.* **549**, 959.
Gardner F.F., Whiteoak J.B. (1966) *Annnu. Rev. Astron. Astrophys.* **4**, 245.
Haverkorn M., Heitsch F. (2004) submitted to *Astron. Astrophys.*
Haverkorn M., Katgert P., De Bruyn A.G. (2003a) to be published in *Astron. Astrophys.*
Haverkorn M., Katgert P., De Bruyn A.G. (2003b) *Astron. Astrophys.* **403**, 1031.
Haverkorn M., Katgert P., De Bruyn A.G. (2003c) *Astron. Astrophys.* **404**, 233.
Haverkorn M., Katgert P., De Bruyn A.G., (2003d) to be published in*Astron. Astrophys.*
Haverkorn M., Katgert P., De Bruyn A.G. (2000) *Astron. Astrophys.* **356**, 13.
Heiles C. (1996) in *Polarimetry of the interstellar medium*, eds. W.G. Roberge & D.C.B. Whittet, ASP Conf. Ser. Vol. **97**, p. 457.
Sokoloff D.D., Bykov A.A., Shukurov A., Berkhuijsen E.M., Beck R., Poezd A.D. (1998) *Mon. Not. R. Astron. Soc.* **299**, 189.
Stone J.M., Norman M.L. (1992a) *Astrophys. J. Suppl.* **80**, 753.
Stone J.M., Norman M.L. (1992b) *Astrophys. J. Suppl.* **80**, 791.
Uyanıker B., Fürst E., Reich W., Reich P., Wielebinski R. (1999) *Astron. Astrophys. Suppl.* **138**, 31.

"The Magnetized Interstellar Medium"
8–12 September 2003, Antalya, Turkey
Eds.: B. Uyanıker, W. Reich & R. Wielebinski

An Additional Source of Turbulence in the Warm ISM of the Inner Galactic Plane ?

M. Haverkorn[1], B. M. Gaensler[1], N. M. McClure-Griffiths[2], John M. Dickey[3] and A. J. Green[4]

[1] Harvard-Smithsonian Center for Astrophysics, 60 Garden Street, Cambridge MA 02138, USA
[2] Australia Telescope National Facility, CSIRO, P.O. Box 76, Epping, NSW 1710, Australia
[3] Department of Astronomy, University of Minnesota, 116 Church Street SE, Minneapolis, MN 55455, USA
[4] School of Physics, University of Sydney, NSW 2006, Australia

Abstract. We present structure functions of the rotation measure (RM) of diffuse Galactic synchrotron emission and of the emission measure (EM) of Hα emission in a test region for the Southern Galactic Plane Survey. The structure functions of RM and EM are remarkably similar: both show a break at a scale of approximately $4'$, where the structure function flattens to a slope of about 0.2 at scales larger than the break. At scales $r \gtrsim 1°$, the structure functions show an anisotropy with position angle on the sky which is believed to be created by a large-scale gradient in thermal electron density and possibly magnetic field across the observed region. The break and flattening of the spectrum can be explained if the radiation propagates through two Faraday screens, most likely the Carina and Local spiral arms. In this interpretation, it can be inferred from the position of the break in the structure function that the warm ISM exhibits structure up to an outer scale of a few parsec. We propose that the observed fluctuations in RM and EM are mainly caused by H II regions around late-type B stars, which are typically a few parsecs in size and sufficiently abundant. These H II regions may constitute the dominant source of turbulence in the inner Galactic plane, as opposed to the Kolmogorov-like turbulence out to scales of hundreds of parsecs observed at high Galactic latitudes.

1 Introduction

Many observations of structure in the warm ionized interstellar medium (ISM) confirm that the warm ISM is turbulent on a wide range of scales. However, the kind of turbulence and the scales it extends to are still under discussion. Armstrong et al. (1995) combined (among others) scattering observations of pulsars and extragalactic sources with rotation measures (RM) of extragalactic sources in a power spectrum of thermal electron density over more than 12 orders of magnitude. They concluded that the electron density has a power law power spectrum of standard incompressible turbulence (Kolmogorov 1941) from scales of AUs to hundreds of parsecs, the so-called "big power law in the sky". This turbulence is most likely driven mainly by supernova explosions on large scales (Mac Low and Klessen 2004), after which energy cascades down to smaller scales until it dissipates at the diffusion scale. However, Minter and Spangler (1996) concluded from extragalactic source RMs that Kolmogorov turbulence exists up to scales of a few parsec and the structure transitions into two-dimensional turbulence on larger scales. These observations have mostly been at high latitudes, while at low latitudes in the inner Galaxy there is evidence for an additional source of fluctuations in electron density and/or magnetic field on degree scales (Simonetti and Cordes 1986, Spangler and Reynolds 1990, Clegg et al. 1992).

In this paper, we present structure functions of RM of the diffuse synchrotron background in a region in the inner Galactic plane. The structure functions give evidence for an additional source of structure in the plane, with an outer scale of a few parsecs. We propose that H II regions are the dominant source of this structure. This work is described in more detail by Haverkorn et al. (2004).

2 The observations

The observations were performed with the Australia Telescope Compact Array (ATCA) at nine frequencies around 1.4 GHz with a resolution of $1'$. The observed field is 28 square degrees in size centered

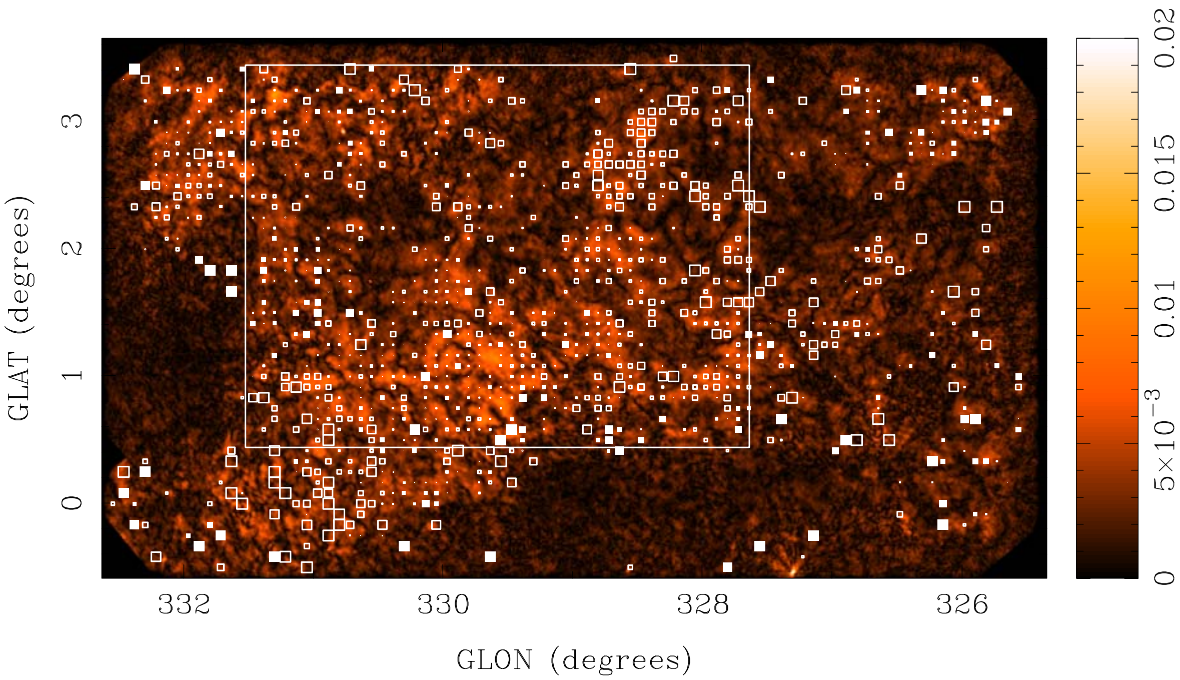

Fig. 1. Rotation measure RM in the SGPS Test Region displayed as squares, superimposed on polarized intensity in color in Jansky beam^{-1}. Open (Filled) squares denote negative (positive) RMs. The length of a square is proportional to the magnitude of the RM for $|RM| < 100$ rad m^{-2}, and constant for $|RM| \geq 100$ rad m^{-2}. RM values are only displayed if the signal-to-noise is S/N > 5 and the reduced χ^2 is $\chi^2_r < 2$. Only the RM in one in nine independent beams is shown for clarity. The rectangular box drawn in the figure is the area over which structure functions are computed.

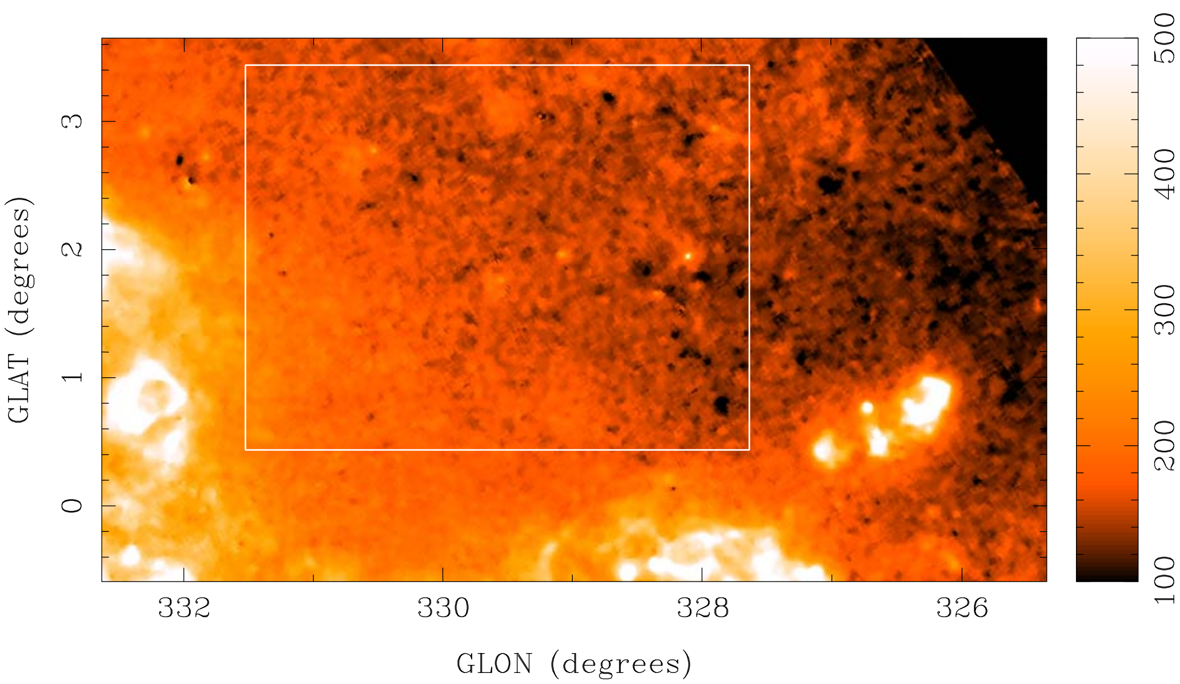

Fig. 2. Hα emission in the SGPS Test Region, from the Southern H-Alpha Sky Survey Atlas (Gaustad et al. 2001). The scale is in deciRayleighs (1 Rayleigh = $10^6/4\pi$ photons cm^{-2} s^{-1} sr^{-1}), the resolution is 0$'\!$.8 and the box is the same as in Fig. 1.

at $(l, b) = (329^\circ\!.0, 1^\circ\!.5)$ and serves as a test region for the Southern Galactic Plane Survey (SGPS, McClure-Griffiths et al. 2001, Gaensler et al. 2001). The region is displayed in Fig. 1, where the color map denotes the polarized intensity P in Jansky beam^{-1} and the superimposed squares are the RM. The rectangular box denotes the region over which the structure functions are computed, see Sect. 3.

As $RM = 0.81 \int B_{\|} n_e \, ds$ only includes the product of magnetic field parallel to the line of sight $B_{\|}$ and thermal electron density n_e integrated over the line of sight ds, observations which give independent information on the electron density are highly useful. These can be obtained by way of the emission measure $EM = \int n_e^2 \, ds$ from Hα observations. Therefore, we have also included in the analysis Hα observations in the Test Region obtained from the Southern H-Alpha Sky Survey Atlas (Gaustad et al. 2001), shown in Fig. 2.

3 Structure functions

The structure function (SF) of RM is a measure of the amount of structure in RM at a certain length scale $\mathbf{r}$ and is defined as:

$$SF_{RM}(\mathbf{r}) = \langle (RM(\mathbf{x}) - RM(\mathbf{x} + \mathbf{r}))^2 \rangle_{\mathbf{x}},$$

where $\langle \, \rangle_{\mathbf{x}}$ denotes averaging over all positions $\mathbf{x}$ in the field. A similar definition holds for the SF of EM. We compute one-dimensional structure functions as a function of vector $\mathbf{r}$ at a certain position angle α (positive b through positive l). The left hand panels in Fig. 3 show the SFs of RM (top) and EM (bottom) as a function of angular scale r. Plots of position angles from 0° to 180° in steps of 10° have been overlaid in the same plot. Both SFs show a broken power law, with a break at $r = 4'$ ($\log(r) = -1.15$), denoted by the dotted line. SFs for different position angles are very similar on small scales, but deviate on large scales. Linear fits to the slope of the SF at those large scales are shown in the right hand panels of Fig. 3, where the linear fit is taken over the range of scales given by the horizontal line in the left hand panels. Both spectra show an anisotropy in the amount of structure at scales $r \gtrsim 1^\circ$, with a maximum amount of fluctuations at position angle $\alpha \approx -50^\circ$.

The Hα data were median-filtered over 4 pixels to reduce the residuals of point source subtraction, which means that the break in the EM spectrum might be due to resolution. In the unsmoothed data, artifacts from residuals of removed point sources prohibited determination of the SF. However, in the RM data the resolution cannot influence the data on scales $\log(r) \gtrsim -1.5$, therefore the break is physical and not due to resolution.

We argue in Sect. 4 that the anisotropy in the spectrum is due to a large-scale gradient in RM and EM, and in Sect. 5 that the break and flattening of the spectrum is caused by the presence of two Faraday screens along the line of sight.

4 A large-scale gradient

It is tempting to interpret an anisotropy in the slope of the SF as resulting from anisotropic turbulence. Anisotropic turbulence is expected in the warm ISM if a large-scale magnetic field component is present. However, in the Goldreich-Sridhar theory of anisotropic turbulence the power spectrum is predicted to be identical to the Kolmogorov spectrum (Goldreich and Sridhar 1995, 1997). Cho et al. (2002) argue that the turbulence is anisotropic with respect to the *local* magnetic field, so that the anisotropy is averaged out for integration over the line of sight. In addition, anisotropic turbulence would be present on all scales, not just on large scales.

Instead, the anisotropy in slope is most likely caused by a large-scale gradient in RM and EM. The gradient in the direction $\alpha = -50^\circ$ can also be seen in the Hα map (Fig. 2). As |RM| is proportional to EM in this field (Haverkorn et al. 2004), the gradient in RM is directed in the same direction.

This indicates a gradient in thermal electron density across the field, possibly accompanied by a gradient in magnetic field. The gradient is probably due to a nearby diffuse ionized cloud. Due to its large angular scale, we assume the cloud is in the Local Arm. But because of the degeneracy between path length and electron density, we cannot derive a value for the electron density from the observed gradient in EM and RM.

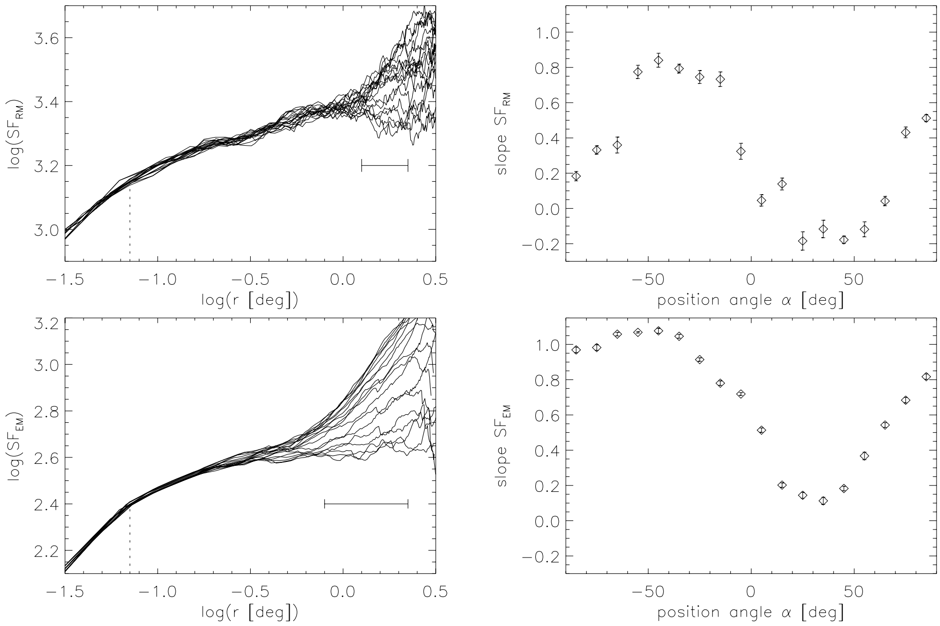

Fig. 3. Left: structure functions of RM (top) and EM (bottom) as a function of angular scale r. One-dimensional SFs for different position angles α from $0°$ to $180°$ in steps of $10°$ are superimposed. Right: slope of the SF from linear fits over the region indicated by the horizontal line in the left hand plots, as a function of position angle α.

5 H II regions as an additional source of structure

For Kolmogorov turbulence, a SF slope of 5/3 is expected (Simonetti et al. 1984). Much flatter slopes, such as the ones observed, can be realized if the observed synchrotron radiation passes through two Faraday screens. This is explained in Fig. 4. In the left hand panel, the solid line shows a sketch of a SF (e.g. of RM) that would result from radiation passing through a Faraday screen which exhibits fluctuations between an inner scale r_i and an outer scale r_o. If two identical screens are placed at different distances, their structure is at different angular scales, as shown in the left hand panel of Fig. 4. The solid line denotes the far screen, and the dashed line the nearby one. In the right hand panel, the SFs of the two screens are added, showing a break and a flattening in the spectrum. The position of the break is at the outer scale of structure of the far screen, whereas the saturation point denotes the outer scale of structure of the nearby screen.

Gaensler et al. (2001) demonstrated that the polarized emission in the Test Region probably originates predominantly from the Crux spiral arm at 3.5 kpc distance. Therefore, the two active Faraday screens are most likely the Carina arm at about 1.5 kpc distance and the Local arm at 100 pc. In this case, the outer scale of structure of the Carina arm corresponds to the position of the break, so that $r_{o,far} \approx 2$ pc. A lower limit for the saturation point is the scale at which the gradient starts to dominate, i.e. $r_{o,near} \gtrsim 1.7$ pc.

This conclusion agrees with earlier studies that found an additional source of turbulence in the inner Galactic plane, from the RM and scattering of pulsars and extragalactic sources in the plane (Simonetti and Cordes 1986, Clegg et al. 1992, Rao and Ananthakrishnan 1984, Dennison et al. 1984, Cordes et al. 1985). Haverkorn et al. (2003) presented SFs from diffuse polarized emission in two fields at intermediate latitudes. As their observations were taken at 350 MHz, the polarized emission they observe only originates nearby, so that their line of sight is mostly through the disk as well. They find flat SFs on scales down to $5'$, possibly with a break at a scale of ~ 2 pc. Furthermore, Spangler and Reynolds (1990) derived from Hα observations of eight extragalactic sources and the assumption that turbulence in the additional component of the gas is strong that the additional component of structure must have an outer scale of a parsec. Armstrong et al. (1995) also noted that the warm ISM is predicted to fill a significant fraction of space as shells of partially ionized gas with a typical scale

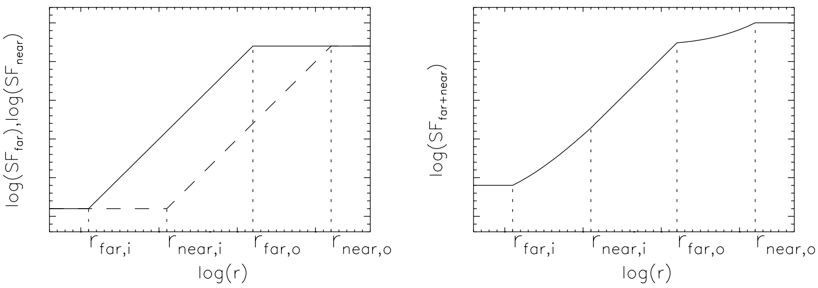

Fig. 4. Left: sketches of two identical structure functions of fluctuations in Faraday screens at different distances: far (solid) and nearby (dashed). Structure is present on scales between the inner scale r_i and the outer scale r_o. Right: sum of the two structure functions, showing a break at the outer scale of the far screen, and a flattening of the spectrum.

of 2 pc. In the external galaxy NGC 6946, Ehle and Beck (1993) modeled the ionized gas by clouds with a typical scale of about one parsec and an electron density of 5 cm^{-3}.

We propose that the source for the additional structure in the Galactic plane is H II regions of mainly late-type B and A0 stars, which are the most abundant stars with significant H II regions. The structure can be caused by the discrete boundaries of the Strömgren spheres themselves, by the turbulence they cause in their environment, by turbulence inside the H II regions, or by a combination of these, although Joncas (1999) argues that turbulence in the interior of H II regions does not operate on scales larger than ~ 0.1 pc.

We tested if H II regions around late-type B stars are sufficiently abundant to be the dominant source of turbulence in the plane with a three-dimensional model volume. H II regions around B3 to A0 stars were distributed randomly in this volume according to the Present Day Mass Function of Miller and Scalo (1979), with radii from Prentice and Ter Haar (1969) (who assume an average density $n = 1$ cm^{-3}). Earlier-type stars were excluded because of their scarceness, whereas stars later than A0 have negligible H II regions. We assumed only stars in the Local and Carina arms, a thickness of the arms of 160 pc (twice the scale height of 80 pc), and the Sun at the outer edge of the Local Arm. The upper plot of Fig. 5 shows a two-dimensional cut through the model volume, where the observer is at $(x, y) = (0, 0)$ and x is the distance along the line of sight. The dashed lines denote the field of view of the rectangular box in Fig. 1. The circles give the individual sizes of the H II regions. The lower left plot shows the spatial density of H II regions as a function of their radius. The fraction of the path length passing through an H II region in parsecs, for all lines of sight at a resolution of $1'$, is shown in the lower right panel. As the average radius of an H II region is a few parsecs, almost all lines of sight pass through several H II regions. Therefore the H II regions around B3 to A0 stars seem to be abundant enough to constitute the main source of structure in the inner Galactic plane.

6 Conclusions

Structure functions of RM from the Galactic synchrotron background, and of EM from Hα emission in the SGPS Test Region are very similar. Both structure functions show similar broken power law spectra at scales $r \lesssim 1°$, where the break is at $r = 4'$, and the spectrum flattens to ~ 0.2 at scales above the break. For the largest scales $r \gtrsim 1°$, both structure functions show an anisotropy in the slope with position angle. The anisotropy in the slope indicates a large-scale gradient of electron density and possibly magnetic field across the field of view at position angle $\alpha \approx -50°$ (positive b through positive l). The break and the flattening of the spectrum can be explained by the superposition of two structure functions of Faraday screens which correspond to the Carina and Local spiral arms. In this interpretation, the outer scale of structure in the spiral arms is approximately 2 pc (which is a lower limit for the outer scale in the Local arm). We propose that these fluctuations in thermal electron density (and possibly magnetic field) are mainly caused by individual H II regions in the spiral arms of late-type B and A0 stars. These are abundant enough to be the dominant source of structure in the warm ISM in the Galactic plane.

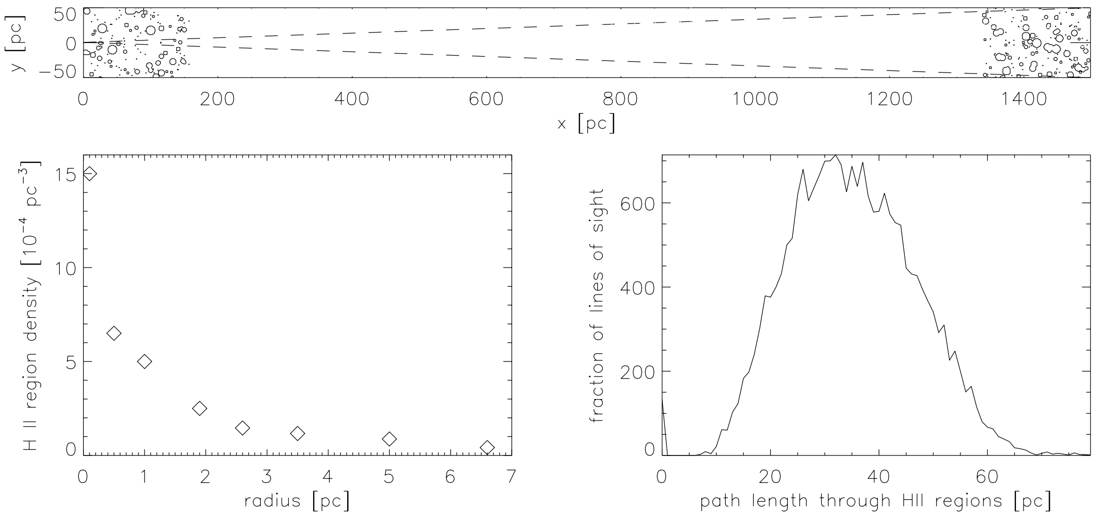

Fig. 5. Top: Cut through a model volume containing B3 to A0 stars randomly distributed in the Local and Carina spiral arms according to the Present Day Mass Function of Miller and Scalo (1979). Circles denote the size of the H II regions around these stars. The observer is at $(x, y) = (0, 0)$ where x is the distance along the line of sight and the dashed lines denote the field of view. Bottom: Spatial density of H II regions against their radius (left), and the amount of a single line of sight that goes through H II regions for all lines of sight in the field, in pc.

Acknowledgments

The Australia Telescope is funded by the Commonwealth of Australia for operation as a National Facility managed by CSIRO. The Southern H-Alpha Sky Survey Atlas (SHASSA) is supported by the National Science Foundation. MH and BMG acknowledge the support of NSF grant AST-0307358.

References

Armstrong J.W., Rickett B.J., Spangler S.R. (1995) *Astrophys. J.* **443**, 209.

Cho J., Lazarian A., Vishniac E.T. (2002) *Astrophys. J.* **564**, 291.

Clegg A.W., Cordes J.M., Simonetti J.M., Kulkarni S.R. (1992) *Astrophys. J.* **386**, 143.

Cordes J.M., Weisberg J.M., Boriakoff V. (1985) *Astrophys. J.* **288**, 221.

Dennison B., Broderick J.J., Thomas M., Booth R.S., Brown R.L., Condon J.J. (1984) *Astron. Astrophys.* **135**, 199.

Ehle M., Beck R. (1993) *Astron. Astrophys.* **273**, 45.

Gaensler B.M., Dickey J.M., McClure-Griffiths N.M., Green A.J., Wieringa M.H., Haynes R.F. (2001) *Astrophys. J.* **549**, 959.

Gaustad J.E., McCullough P.R., Rosing W., Van Buren D. (2001) *Publ. Astron. Soc. Pac.* **113**, 1326.

Goldreich P., Sridhar S. (1997) *Astrophys. J.* **485**, 680.

Goldreich P., Sridhar S. (1995) *Astrophys. J.* **438**, 763.

Haverkorn M., Gaensler B.M., McClure-Griffiths N.M., Dickey, J.M., Green A.J. (2004), submitted to *Astrophys. J.*

Haverkorn M., Katgert P., de Bruyn A.G. (2003) *Astron. Astrophys.* **403**, 1045.

Joncas G. (1999), in *Proceedings of the 2nd Guillermo Haro Conference, Interstellar Turbulence*, eds. J. Franco & A. Carraminana, Cambridge University Press, p. 154.

Kolmogorov A.N., (1941) Dokl. Akad. Nauk SSSR **30**, 301.

Mac Low M.-M., Klessen R.S. (2004) *Rev. Mod. Phys.*, in press (astro-ph/0301093).

McClure-Griffiths N.M., Green A.J., Dickey J.M., Gaensler B.M., Haynes R.F., Wieringa M.H. (2001) *Astrophys. J.* **551**, 394.

Miller G.E., Scalo J.M. (1979) *Astrophys. J., Suppl. Ser.* **41**, 513.

Minter A.H., Spangler S.R. (1996) *Astrophys. J.* **458**, 194.

Prentice A.J.R., Ter Haar D. (1969) *Mon. Not. R. Astron. Soc.* **146**, 423.

Rao A.P., Ananthakrishnan S. (1984) *Nature* **312**, 707.

Simonetti J.H., Cordes J.M. (1986) *Astrophys. J.* **310**, 160.

Simonetti J.H., Cordes J.M., Spangler S.R. (1984) *Astrophys. J.* **284**, 126.

Spangler S.R., Reynolds R.J. (1990) *Astrophys. J.* **361**, 116.

"The Magnetized Interstellar Medium"
8–12 September 2003, Antalya, Turkey
Eds.: B. Uyanıker, W. Reich & R. Wielebinski

Faraday Rotation and Depolarization of Galactic Radio Emission in the Magnetized Interstellar Medium

E. N. Vinyajkin

Radiophysical Research Institute (NIRFI),
25 B. Pecherskaya st., Nizhny Novgorod, 603950, Russia

Abstract. A joint action of depth and bandwidth depolarization in the interstellar medium is considered using a model of N homogeneous synchrotron layers with Faraday rotation. The bandwidth depolarization can be used in multifrequency polarimetric observations of Galactic diffuse synchrotron radio emission to investigate the interstellar ionized medium and magnetic field in the direction to the Faraday-thick objects of known distances.

1 Introduction

Faraday rotation and depolarization have considerable impact on the angular pattern and frequency dependence of the position angle and brightness temperature of the linearly polarized component of the diffuse Galactic synchrotron radio emission. This effect increases with the distance from which we receive the linearly polarized radio emission. The observing frequency, bandwidth and beamwidth play important roles. Faraday depolarization may be caused by: 1) differential Faraday rotation along the line of sight when synchrotron emission and Faraday rotation are mixed (depth or front-back depolarization), 2) differential Faraday rotation in the receiver bandwidth (bandwidth depolarization), and 3) difference of Faraday rotation (and also intrinsic position angles) within the beamwidth (beamwidth depolarization). Depth and bandwidth depolarizations act at sufficiently low frequencies even in the case of a homogeneous radiation region and infinitely narrow antenna beam. Here we consider a joint action of depth and bandwidth depolarization in the interstellar medium using simple models of the regions with the synchrotron radio emission and Faraday rotation. We assume that 1) the receiver bandwidth $\Delta\nu \ll \nu_0$ (ν_0 is the central frequency), 2) the receiver frequency response is rectangular

$$\begin{aligned} \mathcal{F}(s) &= 1, \quad \text{if} \quad |s| \le \frac{\Delta\nu}{2\nu_0}\,, \\ \mathcal{F}(s) &= 0, \quad \text{if} \quad |s| > \frac{\Delta\nu}{2\nu_0}\,, \end{aligned} \tag{1}$$

where $s = (\nu - \nu_0)/\nu_0$, 3) the beam is narrow enough to neglect the difference between position angles of waves coming from different directions.

2 Depth and bandwidth depolarization

2.1 A homogeneous region behind the Faraday screen

Let us consider a model consisting of a radio emission region of extension L along the line of sight with a homogeneous magnetic field and homogeneous space distributions of relativistic and thermal electrons and some other object located in front of it with substantial Faraday rotation and nonpolarized or negligibly small self-emission. Such an object can be an H II region, a magnetic bubble (Vallée, 1984), a planetary nebula, an external part of a molecular cloud (Uyanıker & Landecker, 2002; Wolleben & Reich, this volume), a depolarized supernova remnant (SNR), the solar corona (Soboleva & Timofeeva, 1983; Mancuso & Spangler, 2000), or the Earth ionosphere. The near object is the Faraday screen for the region located behind it. Stokes parameters Q and U in this model account for depolarization in the rectangular bandwidth (1) (Vinyajkin & Krajnov, 1989)

$$\begin{aligned} Q &= \frac{P_0 I}{2\phi\lambda^2}\Big(F\left[2(\phi+\phi_s)\,\lambda^2\delta\right]\sin\big\{2\left[\chi_0+(\phi+\phi_s)\,\lambda^2\right]\big\} - \\ &\quad - F(2\phi_s\lambda^2\delta)\sin\big[2(\chi_0+\phi_s\lambda^2)\big]\Big), \\ U &= \frac{P_0 I}{2\phi\lambda^2}\Big(- F\left[2(\phi+\phi_s)\,\lambda^2\delta\right]\cos\big\{2\left[\chi_0+(\phi+\phi_s)\,\lambda^2\right]\big\} + \\ &\quad + F(2\phi_s\lambda^2\delta)\cos\big[2(\chi_0+\phi_s\lambda^2)\big]\Big), \end{aligned} \tag{2}$$

where P_0 is the intrinsic polarization degree, χ_0 is the intrinsic position angle, I is the intensity, $\phi = 0.81(\mathrm{rad}\cdot\mathrm{m}^{-2}\mathrm{cm}^3\mu\mathrm{G}^{-1}\mathrm{pc}^{-1})N_e B_\parallel L$ is the Faraday depth of the radiation region, N_e is the electron density, $B_\parallel = \mathbf{Bk}/k$ is the component of the magnetic field $\mathbf{B}$ along the line of sight ($\mathbf{k}$ is the wave vector, $k = 2\pi/\lambda$ is the wave number), $\phi_s = 0.81(\mathrm{rad}\cdot\mathrm{m}^{-2}\mathrm{cm}^3\mu\mathrm{G}^{-1}\mathrm{pc}^{-1})(N_e)_s B_{\parallel s} L_s$ is the Faraday screen depth, $\delta = \Delta\nu/\nu$, and

$$F(2x\lambda^2\delta) = \frac{\sin(2x\lambda^2\delta)}{2x\lambda^2\delta}\,. \tag{3}$$

2.2 N different homogeneous layers

Now let us consider a more general model consisting of N different homogeneous layers (Sokoloff et al., 1998), each of them characterized by three parameters: the intensity I_i, Faraday depth ϕ_i, and intrinsic position angle χ_{0i}, where $i = 1, 2, \ldots, N$ and the farthest region has $i = 1$. If one of the layers is not a source of linearly polarized radio emission and only rotates the polarization plane, then $I_i = 0$. The intrinsic polarization degree of any emitting layer is the same and equals to P_0.

Expressions for Stokes parameters of the N-layer model are easily obtained from (2) and (3), if we take into account that all regions from $i+1$ up to N play the role of the Faraday screen for the i-region and rotate the polarization plane by the angle $\left(\sum_{j=i+1}^{N}\phi_j\right)\lambda^2$. Because the Stokes parameters are additive for noncoherent radio emission, the values of Q_N, U_N for the N-layer region can be obtained by summing up over all N components (Vinyajkin et al., 2002):

$$\begin{aligned} Q_N &= P_0\sum_{i=1}^{N}\frac{I_i}{2\phi_i\lambda^2}\left(F\left[2\left(\phi_i+\sum_{j=i+1}^{N}\phi_j\right)\lambda^2\delta\right]\sin\left\{2\left[\chi_{0i}+\left(\phi_i+\sum_{j=i+1}^{N}\phi_j\right)\lambda^2\right]\right\} - \right.\\ &\qquad\left. - F\left[2\left(\sum_{j=i+1}^{N}\phi_j\right)\lambda^2\delta\right]\sin\left\{2\left[\chi_{0i}+\left(\sum_{j=i+1}^{N}\phi_j\right)\lambda^2\right]\right\}\right), \\ U_N &= P_0\sum_{i=1}^{N}\frac{I_i}{2\phi_i\lambda^2}\left(-F\left[2\left(\phi_i+\sum_{j=i+1}^{N}\phi_j\right)\lambda^2\delta\right]\cos\left\{2\left[\chi_{0i}+\left(\phi_i+\sum_{j=i+1}^{N}\phi_j\right)\lambda^2\right]\right\} + \right.\\ &\qquad\left. + F\left[2\left(\sum_{j=i+1}^{N}\phi_j\right)\lambda^2\delta\right]\cos\left\{2\left[\chi_{0i}+\left(\sum_{j=i+1}^{N}\phi_j\right)\lambda^2\right]\right\}\right). \end{aligned} \tag{4}$$

If $\delta \to 0$, $F \to 1$, and Eqs. (4) correspond to eq. (9) from Sokoloff et al. (1998).

$N = 1$

In the case of a single homogeneous layer ($N = 1$) we get from (4):

$$Q_1 = P_0 \frac{I}{2\phi\lambda^2} \left(\frac{\sin(2\phi\lambda^2\delta)}{2\phi\lambda^2\delta} \sin\left[2\left(\chi_0 + \phi\lambda^2\right)\right] - \sin 2\chi_0 \right),$$

$$U_1 = P_0 \frac{I}{2\phi\lambda^2} \left(-\frac{\sin(2\phi\lambda^2\delta)}{2\phi\lambda^2\delta} \cos\left[2\left(\chi_0 + \phi\lambda^2\right)\right] + \cos 2\chi_0 \right). \tag{5}$$

The depolarization factor $DP = \sqrt{Q^2 + U^2}/IP_0 = P/P_0$, where P is the observed degree of polarization, is equal to (Vinyajkin & Krajnov, 1989; Vinyajkin & Razin, 2002)

$$DP_1 = \frac{1}{2\,|\phi|\,\lambda^2} \left(\left[\frac{\sin(2\phi\lambda^2\delta)}{2\phi\lambda^2\delta} \right]^2 - 2\,\frac{\sin(2\phi\lambda^2\delta)}{2\phi\lambda^2\delta} \cos(2\phi\lambda^2) + 1 \right)^{1/2}. \tag{6}$$

The dotted lines in Figs. 1 and 2 represent the dependencies of the depolarization factor (6) on $\phi\lambda^2/2$ in the intervals $0 \div 10$ and $70 \div 25\pi$, respectively, for the typical value $\delta = 0.01$. The solid lines in these figures show the dependencies of the observed position angle $\chi_{1\,\mathrm{obs}}$ on $\phi\lambda^2/2$[1]

$$\chi_{1\mathrm{obs}} = \frac{1}{2}\,\mathrm{angle}\,(Q_1, U_1), \tag{7}$$

where angle (x, y) gives the angle in radians between the axis x (vertical axis Q) and the vector with coordinates x, y (polarization vector on the plane Q, U). It is seen from Eqs. (5) and (6) and from Figs. 1 and 2 that the oscillation amplitude of the position angle near the value $(\chi_0 + \pi/2)/2 = \pi/4$ (assuming $\chi_0 = 0$) decreases with increasing $\phi\lambda^2/2$, and at $\phi\lambda^2/2 = \pi/4\delta = 25\pi$ the position angle $\chi_{1\,\mathrm{obs}} = \pi/4$, $DP_1 = \delta/\pi = (1/\pi)\%$.

In the limit of infinitely narrow band $\delta \ll 1/2\,|\phi|\,\lambda^2$ (we have assumed $\delta \ll 1$) Eqs. (5) transform to

$$Q_1(\delta \to 0) = P_0 I\,\frac{\sin\phi\lambda^2}{\phi\lambda^2} \cos\left[2\left(\chi_0 + \frac{\phi}{2}\,\lambda^2\right)\right],$$

$$U_1(\delta \to 0) = P_0 I\,\frac{\sin\phi\lambda^2}{\phi\lambda^2} \sin\left[2\left(\chi_0 + \frac{\phi}{2}\,\lambda^2\right)\right], \tag{8}$$

and (6) transforms into the known formula for the depolarization factor of a homogeneous synchrotron layer with rotation in the limit of the infinitely narrow bandwidth and beam (Razin, 1956)

$$DP_1(\delta \to 0) = \left| \frac{\sin\phi\lambda^2}{\phi\lambda^2} \right|. \tag{9}$$

The position angle corresponding to Stokes parameters (8) equals to (Razin, 1956; Burn, 1966; Vinyajkin, 1995)

$$\chi_1(\delta \to 0) = \chi_0 + \frac{\phi}{2}\,\lambda^2 - \frac{\pi}{2}\,E(\phi\lambda^2/\pi), \tag{10}$$

where $E(x) = -E(-x)$ is the integral part of argument x. The position angle values of (10) may come out of the interval $0 \div 180°$, for example, if $\chi_0 > \pi/2$ and $\phi > 0$. To calculate the observed values $\chi_{1\,\mathrm{obs}}$ one has to use Eq. (7) with the Stokes parameters from (8). Figures 3 and 4 give plots of $\chi_{1\,\mathrm{obs}}$ $(\delta \to 0)$ as dependent on $(\phi/2)\,\lambda^2$ (solid lines) for the values of χ_0, respectively, $\pi/4$ and $3\pi/4$ (dashed

[1] Here the observed values of the position angle are those measured in the interval $0 \div \pi$ and counted counter-clockwise from the vertical. In Figs. 1 and 2 the observed position angles are identical with the true ones. In the general case the observed value of the position angle may differ from the true one by $\pm n\pi$ $(n = 0, 1, 2, \ldots)$.

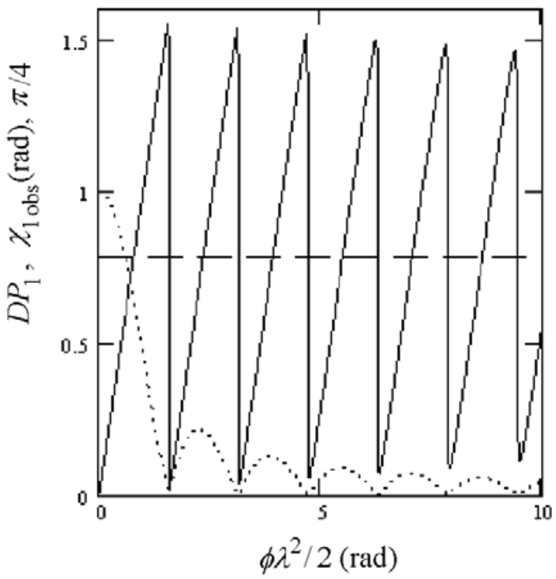

Fig. 1. The depolarization factor DP_1 (dotted line), the observed position angle $\chi_{1\,\mathrm{obs}}$ (solid line), and the number $\pi/4$ (dashed line), see text.

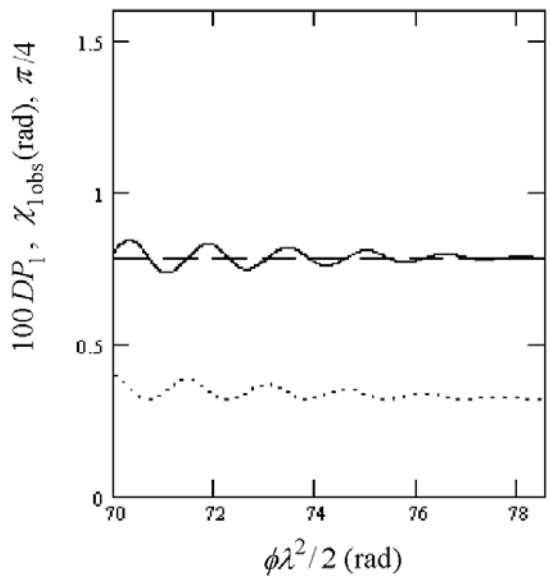

Fig. 2. Same as Fig. 1, but for the $\phi\lambda^2/2$ interval 70 to 25π instead of 0 to 10, and 100 DP_1 instead of DP_1.

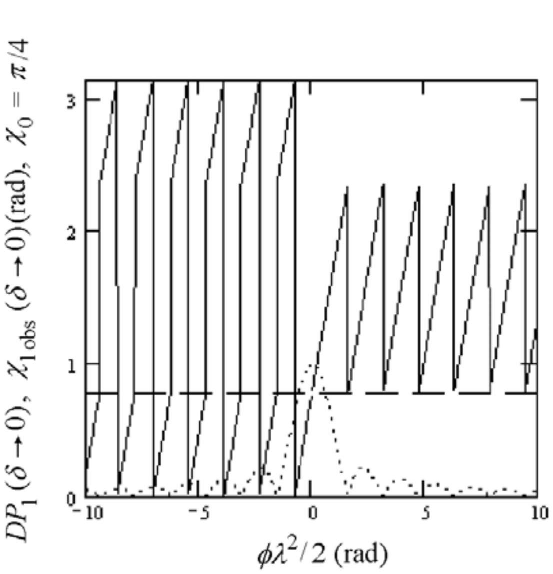

Fig. 3. The depolarization factor DP_1 ($\delta \to 0$) (dotted line), the observed position angle $\chi_{1\,\mathrm{obs}}$ ($\delta \to 0$) (solid line), and $\chi_0 = \pi/4$ (dashed line).

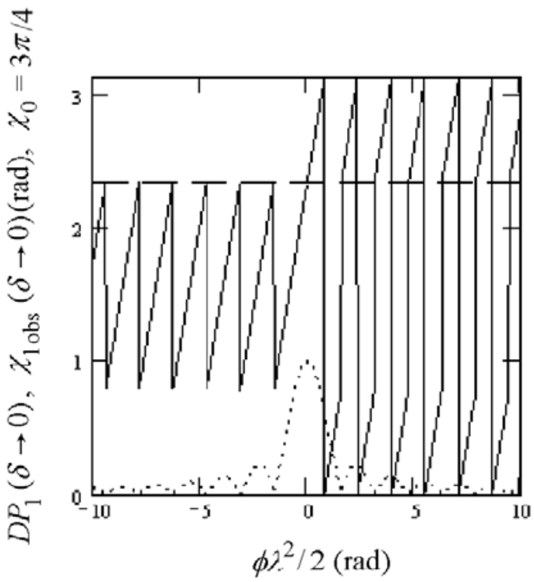

Fig. 4. Same as Fig. 3, but for $\chi_0 = 3\pi/4$.

lines). The depolarization factor (9) is shown by dotted lines. The rotation measure $RM = \phi/2$ and peculiarities of its determination in this model have been considered in detail by Vinyajkin (1995). The model of a homogeneous layer was used by Vinyajkin (1995) to give the interpretation of a deep minimum of the polarization brightness temperature and a $\pi/2$-jump of the position angle observed in the North Polar Spur in the direction with coordinates $\alpha_{1950} = 16^{\mathrm{h}}\,48^{\mathrm{m}}$, $\delta_{1950} = 14^\circ$ at 960 MHz (Vinyajkin, 1995).

$N = 3$

Let us consider the model of the region consisting of two homogeneous synchrotron polarized layers and the Faraday screen between them. In this case the contribution of the far layer ($i = 1$) in the observed polarized radio emission becomes 0 at some relatively low frequency because of its bandwidth depolarization. If the distance to the Faraday screen is known, we can estimate the extension of the near synchrotron layer. As an example, let us consider the following model parameters: $I_1/I = I_3/I = 0.5$, $I_2 = 0$, $\chi_{01} = \chi_{03} = 0$, $\phi_1 = \phi_3 = 0$, $\phi_2 = 100$ rad/m^2. The contribution of the far layer becomes 0 and, hence, the depolarization factor becomes 0.5 (see Figs. 5 and 6) at the minimum wavelength

$$\lambda_{\min} = \sqrt{\frac{\pi}{2}}\,\frac{1}{\sqrt{\phi_2 \delta}}\,, \qquad (11)$$

which corresponds to the first zero of the function $|\sin(\Delta\chi)/\Delta\chi|$, where $\Delta\chi = 2\phi_2\lambda^2\delta$ is the differential Faraday rotation in the bandwidth. Substituting $\phi_2 = 100$ rad/m^2, $\delta = 0.01$ in (11) we get $\lambda_{\min} \approx 1.25$ m ($\nu_{\max} \approx 240$ MHz). Equation (11) can be used to estimate the cut-off wavelength of the far layer if $\phi_1 \ll \phi_2$. Let us consider some objects. The RM of SNR CTB 104A changes from ~ -80 rad/m^2 in the southeast to $\sim +170$ rad/m^2 in the northwest (Uyanıker et al., 2002). Assuming $\phi_2 \sim 340$ rad/m^2, $\delta = 0.01$ we get from (11) $\lambda_{\min} \sim 0.7$ m ($\nu_{\max} \sim 430$ MHz). At this wavelength this part of the SNR is nearly completely depolarized because of the depth depolarization ($P < 0.4\%$). The RM of the H II region S205 is 250 rad/m^2 (Mitra et al. 2003; Wielebinski & Mitra, this volume). In this case $\phi_2 = 250$ rad/m^2 and, if $\delta = 0.01$, we get $\lambda_{\min} \approx 0.8$ m ($\nu_{\max} \approx 375$ MHz). Gray et al. (1999) detected a strong beam and bandwidth depolarization across the face of W3 and W4 and immediately near them at 1420 MHz (30 MHz bandwidth).

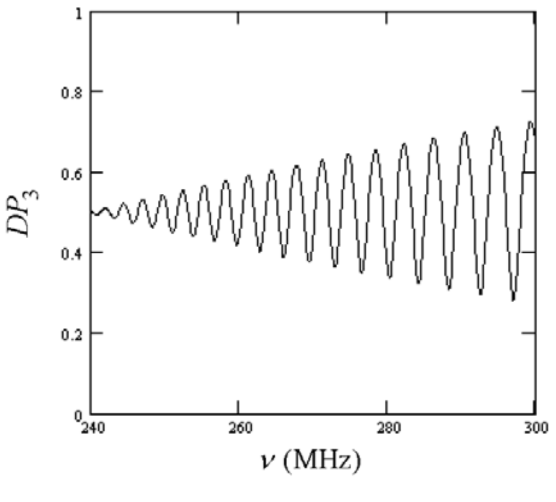

Fig. 5. The depolarization factor DP_3 of the three-layer model (see text) versus frequency in the interval $240 \div 300$ MHz.

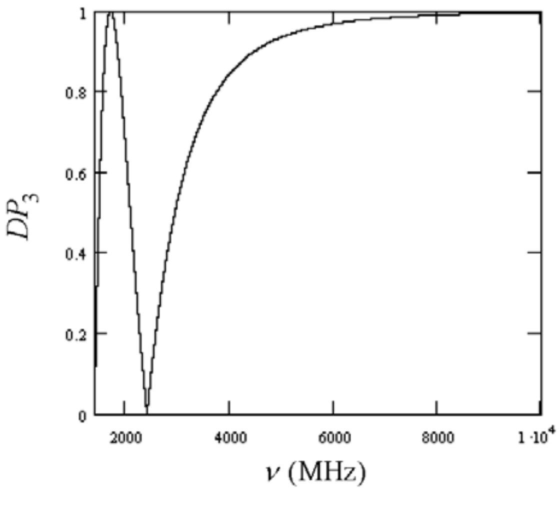

Fig. 6. Same as Fig. 5, but for the frequency interval $1400 \div 10000$ MHz.

Carrying out high angular resolution broadband polarimetric multifrequency observations in the directions to the Faraday screens with known distances it is possible to investigate the interstellar ionized gas and magnetic field along the line of sight. However, interference is a serious problem in carrying out such observations.

3 Conclusion

The bandwidth depolarization can be a useful tool in multifrequency polarimetric observations of Galactic diffuse synchrotron radio emission to investigate the interstellar ionized gas and magnetic field in the directions to Faraday-thick objects of known distances.

Acknowledgment

This work has been supported by the International Science and Technology Center under the ISTC project No. 729.

References

Burn, B. J. (1966) *Mon. Not. R. Astron. Soc.* **133**, 67.
Gray, A. D., Landecker, T. L., Dewdney, P. E., Taylor, A. R., Willis, A. G., Normandeau, M. (1999) *Astrophys. J.* **514**, 221.
Mancuso, S., Spangler, S. R. (2000) *Astrophys. J.* **539**, 480.
Mitra, D., Wielebinski, R., Kramer, M., Jessner, A. (2003) *Astron. Astrophys.* **398**, 993.
Razin, V. A. (1956) *Rad. i Elek.* **1**, 846.
Soboleva, N. S., Timofeeva, G. M. (1983) *Soviet Astron. Lett.* **9**, 216.
Sokoloff, D. D., Bykov, A. A., Shukurov A., Berkhuijsen, E. M., Beck, R., Poezd, A. D. (1998) *Mon. Not. R. Astron. Soc.* **299**, 189.
Uyanıker, B., Landecker, T. L. (2002) in *Astrophysical Polarized Backgrounds*, eds. S. Cecchini, S. Cortiglioni, R. Sault, & C. Sbarra, AIP Conf. Proc. 609, (Melville: AIP), p. 15.
Uyanıker, B., Kothes, R., Brunt, C. M. (2002) *Astrophys. J.* **565**, 1022.
Vallée, J. P. (1984) *Astron. Astrophys.* **136**, 373.
Vinyajkin, E. N., Krajnov, I. L. (1989) Preprint of the Radiophysical Research Inst. (NIRFI), Gorky, No. 288.
Vinyajkin, E. N. (1995) *Astron. Rep.* **39**, 599.
Vinyajkin, E. N., Razin, V. A. (2002) in *Astrophysical Polarized Backgrounds*, eds. S. Cecchini, S. Cortiglioni, R. Sault, & C. Sbarra, AIP Conf. Proc. 609, (Melville: AIP), p. 26.
Vinyajkin, E. N., Paseka, A. M., Teplykh, A. I. (2002) *Radiophysics and Quantum Electronics* **45**, 102.

"The Magnetized Interstellar Medium"
8–12 September 2003, Antalya, Turkey
Eds.: B. Uyanıker, W. Reich & R. Wielebinski

Modelling Faraday Screens in the Interstellar Medium*

Maik Wolleben and Wolfgang Reich

Max-Planck-Institut für Radioastronomie, Auf dem Hügel 69, 53121 Bonn, Germany

Abstract. Maps of Galactic polarized continuum emission at 1408, 1660, and 1713 MHz towards the local Taurus molecular cloud complex were made with the Effelsberg 100-m telescope. Minima in the polarized emission which are located at the boundary of a molecular cloud were detected. Beside high rotation measures and unusual spectral indices of the polarized intensity, these features are associated with the molecular gas. At the higher frequencies the minima get less distinct. We have modelled the multi-frequency observations by placing magneto-ionic Faraday screens at the distance of the molecular cloud. In this model Faraday rotated background emission adds to foreground emission towards these screens. The systematic variation of the observed properties is the result of different line-of-sight lengths through the screen assuming spherical symmetry. For a distance of 140 pc to the Taurus clouds the physical sizes of the Faraday screens are of the order of 2 pc. In this paper we describe the data calibration and modelling process for one such object. We find an intrinsic rotation measure of about -29 rad m^{-2} to model the observations. It is pointed out that the observed rotation measure differs from the physical. Further observational constraints from Hα observations limit the thermal electron density to less than 0.8 cm^{-3}, and we conclude that the regular magnetic field strength parallel to the line-of-sight exceeds 20 μG to account for the intrinsic rotation measure.

1 Introduction

Various surveys of Galactic polarized emission revealed an unexpected richness in highly varying structures in the polarized sky as discussed on this conference. In many cases these fluctuations in the polarized intensity and position angle have no counterpart in total intensity. One likely explanation for these observations is polarized background emission modulated by Faraday rotation. However, many emitting and rotating layers may exist along the line-of-sight so that the observed polarization is a superposition of modified background and unmodified foreground emission layers.

The average density of thermal electrons in the Galactic plane is about 0.03 cm^{-3} and the average of the regular magnetic field along the line-of-sight is about 1 to 2 μG (Taylor & Cordes 1993, Goméz et al. 2001). However, local enhancements of n_e are often observed as diffuse H II-regions due to their optical Hα emission occurring from ionization and recombination of hydrogen. At low observing frequencies Faraday rotation is high and the polarization angle of synchrotron radiation is very sensitive to fluctuations in the electron density, Other than Hα emission Faraday rotation depends on electrons from all sorts of elements. Measurements of local conditions of the Galactic magnetic field are not straightforward and often done by exploiting the Zeeman splitting effect. Faraday rotation of polarized radiation is another tool for the investigation of magnetic fields in case the thermal electron density is known.

For a given observing frequency the amount of Faraday rotation is proportional to the product of the electron density times the magnetic field component parallel to the line-of-sight. Fluctuations in either or both lead to changes in the observed polarization angle. Since such fluctuations are often of small spatial extent, one can describe them in terms of Faraday screens. However, the observation of the effect of Faraday screens on polarized background radiation is not straightforward since foreground emission adds vectorially to the modified background. The closer the screen the more apparent its effect, and the key problem is the unknown distance of the Faraday screens. However, distances to the Taurus–Auriga molecular cloud complexes are known to be about 140 ± 20 pc (e.g. Elias 1978) and structures on pc–scales can be resolved with arcmin angular resolution. In addition the Taurus–Auriga

*Based on observations with the Effelsberg 100-m telescope operated by the Max-Planck-Institut für Radioastronomie (MPIfR), Bonn, Germany complex is located at medium latitudes well below the Galactic plane resulting in a relatively short line-of-sight through the Galaxy.

Here, we analyze a map from the $\lambda\,21\,\mathrm{cm}$ *Effelsberg Medium Latitude Survey* (EMLS, see Reich et al., this volume), which shows a number of enhancements and depressions in the polarized intensity apparently related to molecular gas of the Taurus complex. We interpret the coincidence in position and shape as strong evidence for Faraday effects taking place at the distance of the molecular cloud. In order to derive physical properties of the associated Faraday screens we have complemented the$\lambda\,21\,\mathrm{cm}$ survey data of the Taurus–Auriga region by observations at 18 cm wavelength. We modelled the polarization data in order to constrain the physical parameters of the Faraday screens by taking foreground and background emission into account.

2 Observation and Calibration

The $\lambda\,21\,\mathrm{cm}$ EMLS covers the northern Galactic plane in the range of $|b| \leq 20^\circ$ at a frequency of 1.4 GHz. Follow–up observations of a field north of the center of the Taurus molecular cloud complex were carried out at 1660 and 1713 MHz. Total intensities and linear polarization were measured simultaneously with sensitivities of 15 mK (1408 MHz) to 19 mK (1713 MHz) for Stokes I and 8 mK (1408 MHz) to 10 mK (1713 MHz) for Stokes U and Q at angular resolutions of $9\farcm35$ (1408 MHz) to $7\farcm87$ (1713 MHz). The same receiver was used for all three frequencies, but different HF-filters were selected to suppress interferences. The effective bandwidth was 20 MHz for 1408 MHz and 14 MHz for 1660 and 1713 MHz. Fields were mapped two times in orthogonal scanning directions and are fully sampled. 3C 286 served as the main calibrator for total power and polarization data.

Varying ground and atmospheric radiation causes temperature gradients across the map. In order to remove such gradients a linear baseline is subtracted from each subscan. This procedure also removes real sky signals of large extent, which leads to a similar problem like missing zero spacings in synthesis telescope imaging. At 1408 MHz the missing large-scale emission is usually recovered by absolutely calibrated data. For total intensities 1.4 GHz data from the Stockert northern-sky survey (Reich 1982, Reich & Reich 1986) were used. For polarization data we rely so far on the Dwingeloo survey (Brouw & Spoelstra 1976). The final calibration of polarization will be made with the data from the new DRAO 1.4 GHz survey (see Wolleben et al., this volume). Therefore all quantitative results given below should be taken as preliminary. However, other than at 1.4 GHz there exist no absolutely calibrated surveys at 1660 or 1713 MHz and we calibrated the maps in the following way: The temperature spectral index β ($T \propto \nu^\beta$) of Galactic continuum emission was adopted to be $\beta = -2.7$ in the Taurus area (Reich & Reich 1988). We assumed the same spectral index also for the large-scale polarized intensity and calculated an average offset for the 1660 and 1713 MHz maps from the 1408 MHz map. Rotation measures across the Taurus region were determined by Spoelstra (1972) and are very low everywhere varying around zero, and therefore we assumed no position angle difference for the large-scale emission.

The total power maps for all three frequencies show smooth diffuse emission varying mainly with Galactic latitude and a large number of unrelated extragalactic sources, but no structures related to the polarized emission. However, there are numerous small-scale polarization minima obviously related to the molecular gas cloud (see Fig. 1). They show rather clear differences in intensity and polarization angle distribution between 1408 and 1713 MHz. Polarized intensities towards these minima increase at higher frequencies, which is in contrast to the large-scale polarized emission and other obviously unrelated small-scale variations. The variation of the polarization angle with frequency reveals rotations measures of up to 50 $\mathrm{rad\,m^{-2}}$ (see Fig. 2). The 1660 MHz data were used mainly for a consistency check of the modelling as described below.

3 Modelling a Faraday Screen

We have applied a simple model to describe the observed variations in the polarization maps at all three frequencies. In this model, a Faraday screen is modulating background polarized emission passing through it, which adds to a constant foreground emission. The foreground and background emission

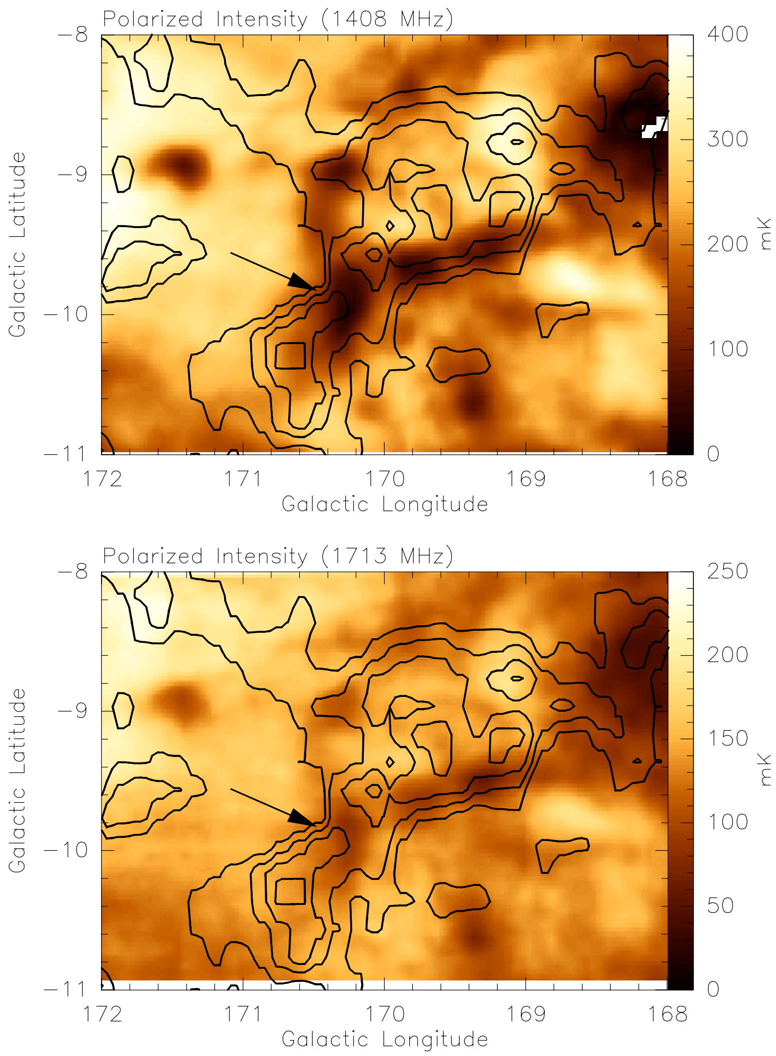

Fig. 1. Maps of the polarized intensity at 1408 (top) and 1713 MHz (bottom) towards a $4 \times 3°$ region north of the center of the Taurus molecular cloud complex. Contours indicate the intensity of the velocity-integrated brightness temperature of ^{12}CO(1-0) emission (Dame et al. 2001). Contour levels are from 9 to 50 K km s^{-1} in steps of 3 K km s^{-1}. The minimum in the polarized intensity modelled as a Faraday screen in Sect. 3 is marked.

is assumed to be constant for all lines-of-sight through the Faraday screen. This seems justified since variations of polarized emission outside the Faraday screens are on larger scales.

At first we define a Faraday screen as an object which can affect the position angle and polarized intensity of polarized background radiation. The effect of the screen will depend on the path length radiation has to pass through it and thus depends on its size and shape. For reasons of simplicity we assume Faraday screens to be spherical objects with constant electron density, homogeneous magnetic field, and radius R. In case of elliptically shaped objects, coordinates were transformed to allow modelling in circular coordinates. The path length through the screen will therefore vary systematically with the observed position. With r as the distance from the center of the screen projected on the sky, the path length L is then given by $L(r) = 2R \cdot (1 - \frac{r^2}{R^2})^{1/2}$ and the fractional path length $l(r) = \frac{L(r)}{2R}$.

A Faraday screen may decrease the degree of polarization by beam depolarization, which seems possible due to the relatively small spatial extent of the Faraday screens discussed here. We assume any depolarization to increase linearly with the fractional path length $l(r)$ and express $DP_{\text{screen}}(r)$ by:

$$DP_{\text{screen}}(r) = l(r) \cdot (1 - DP_0) + DP_0 \tag{1}$$

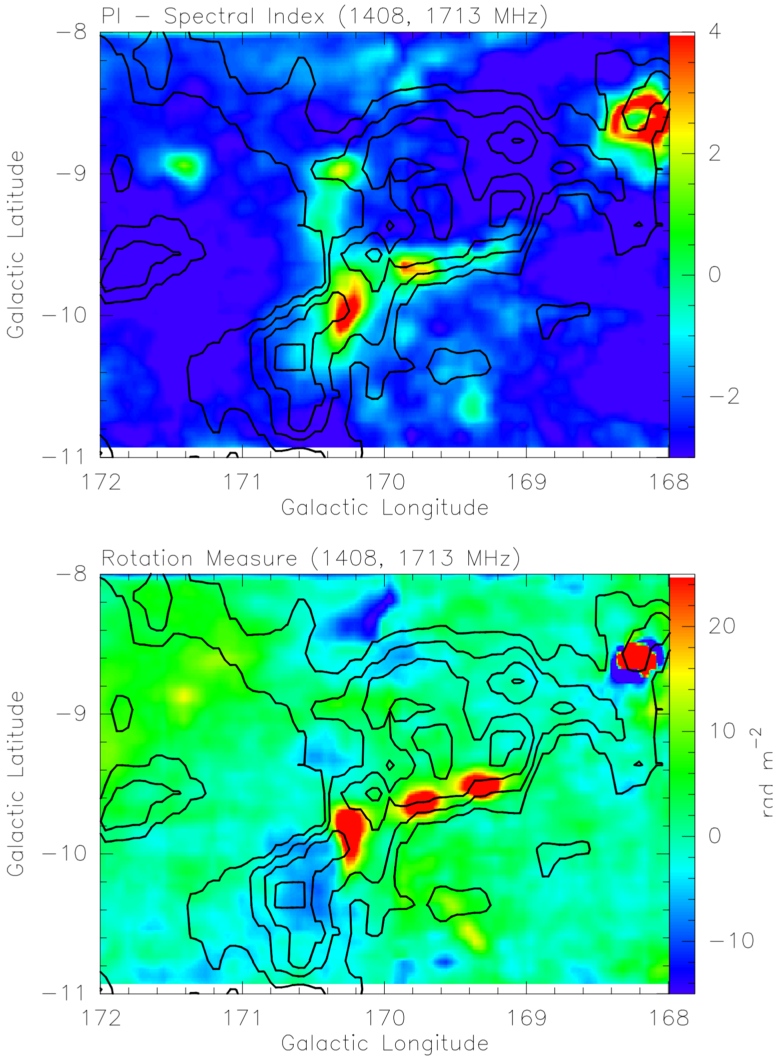

Fig. 2. Maps show the spectral index distribution of the polarized intensity (top) and the rotation measure distribution derived from the polarization angle rotation between 1408 and 1713 MHz (bottom). Contours are the same as in Fig. 1.

with DP_0 the maximum intrinsic depolarization at $r = 0$. In this notation $DP = 1$ means no depolarization and $DP = 0$ complete depolarization of the background radiation.

A Faraday screen also rotates the position angle of linearly polarized background radiation. The amount of Faraday rotation is given by $\Delta PA = RM \cdot \lambda^2$ with the rotation measure $RM\,(\mathrm{rad\ m^{-2}}) = 0.81\,B_{\|}\,(\mu\mathrm{G})\,n_\mathrm{e}\,(\mathrm{cm^{-3}})\,l\,(\mathrm{pc})$. The rotation measure of the screen depends on the fractional path length $l(r)$ and can be expressed as follows:

$$RM_\mathrm{screen}(r) = RM_0 \cdot l(r) \tag{2}$$

with RM_0 the maximum intrinsic rotation measure at $r = 0$.

Depolarization and Faraday rotation are the two effects a Faraday screen might cause. The background polarized emission gets modified in a systematic way as a function of r and can be expressed by:

$$\begin{aligned} PI_\mathrm{mod}(r) &= DP_\mathrm{screen}(r) \cdot PI_\mathrm{back} \\ PA_\mathrm{mod}(r) &= RM_\mathrm{screen}(r) \cdot \lambda^2 + PA_\mathrm{back} \end{aligned} \tag{3}$$

The observed polarization is the superposition of the modified background and the foreground polarization, which in that case is a vector rather than a scalar addition as in the case of total

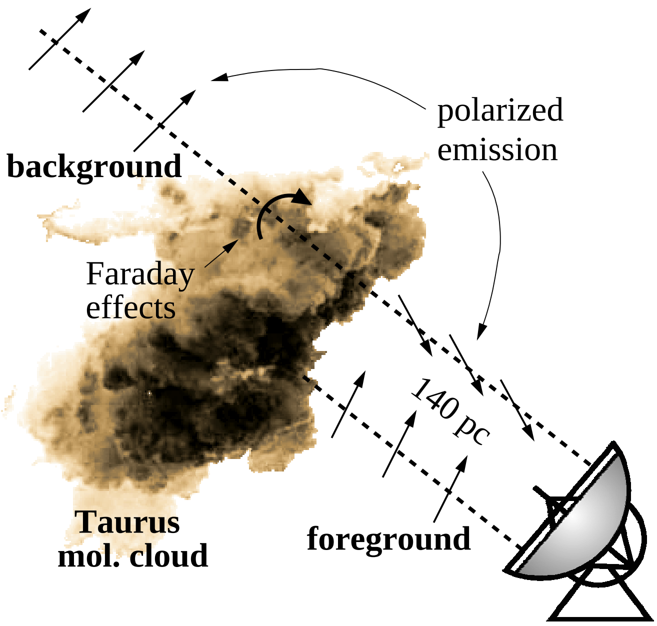

Fig. 3. Sketch of a Faraday screen showing the configuration of foreground and background polarized emission. Here, the Faraday screen is located at the surface of a molecular cloud. The observer measures the superposition of polarized emission from an unmodified foreground and a Faraday rotated and possibly depolarized background. The distance to the Taurus molecular clouds is 140 pc.

intensities. This means to add U and Q and calculate from these values the resulting PI and PA. With

$$\begin{aligned} U_{\rm mod}(r) &= PI_{\rm mod}(r) \cdot \sin(2PA_{\rm mod}(r)) \\ Q_{\rm mod}(r) &= PI_{\rm mod}(r) \cdot \cos(2PA_{\rm mod}(r)) \end{aligned} \tag{4}$$

The observable polarization calculates then by:

$$\begin{aligned} PI_{\rm obs}(r) &= \sqrt{(U_{\rm fore} + U_{\rm mod}(r))^2 + (Q_{\rm fore} + Q_{\rm mod}(r))^2} \\ PA_{\rm obs}(r) &= \frac{1}{2}\arctan\left(\frac{U_{\rm fore}+U_{\rm mod}(r)}{Q_{\rm fore}+Q_{\rm mod}(r)}\right). \end{aligned} \tag{5}$$

Fitting the two modelled observables $PI_{\rm obs}$ and $PA_{\rm obs}$ to the measured polarized intensities and angles towards the Faraday screens is done by optimizing the four free parameters of the model: $PI_{\rm fore}$, $PA_{\rm fore}$, RM_0, and DP_0. At $r \geq 1$ the pure superposition of background and foreground polarization must result in the measured polarization outside the screen. This limiting condition constrains the background polarization for $r < 1$. The model correctly reproduces the observed high spectral indices of polarized intensities, the rotation measures, as well as the observed variation in polarized intensity and angle (see Fig. 4). We find the following best-fit parameters for the Faraday screen marked in Fig. 1: $PI_{\rm fore} \sim 150$ mK, $PA_{\rm fore} \sim -1°$, $PI_{\rm back} \sim 130$ mK, $PA_{\rm back} \sim -14°$, $RM_0 \sim -29.3\,{\rm rad\,m^{-2}}$, and $DP_0 = 1$. These values describe the foreground and background emission, as well as the rotation measure (see next paragraph) and depolarization at 1.4 GHz. The other Faraday screens which can be identified will be discussed in a subsequent paper (Wolleben & Reich 2004).

Limitations of this model arise from the simplification of the shape and properties of Faraday screens, which are likely not perfectly elliptical with constant electron density and homogeneous magnetic field inside, but might be more turbulent or have a small filling factor. However, the absence of depolarization indicates little turbulence within the Faraday screen. Another simplification is that shape and size of the screens were estimated by eyeball based on their appearance in the PI–spectral index map. Finally, Faraday screens can overlap, which was not accounted for, but which is probably the case for the screen fitted here as seen from Fig. 1.

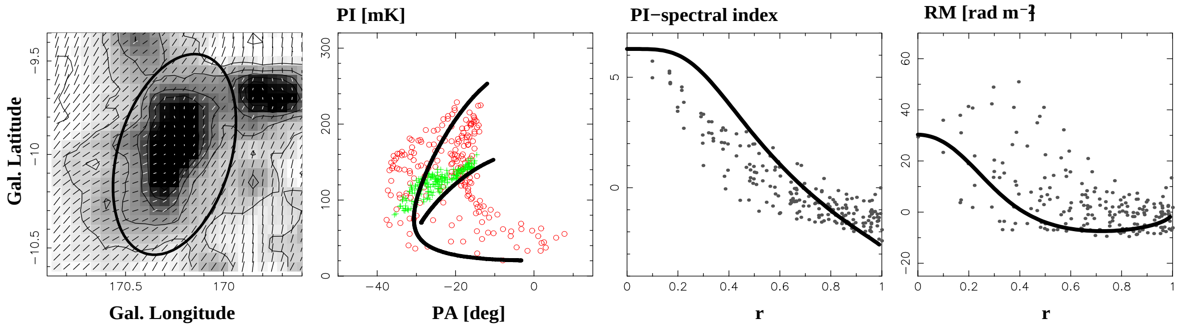

Fig. 4. From left to right are shown: map of the observed spectral index of polarized emission with an ellipse marking the size of the Faraday screen, the PA–PI plot for 1408 MHz (red) and 1713 MHz (green), the observed spectral index of polarized emission, as well as the observed rotation measure versus radius r. The black lines indicate the model-fit.

4 Conclusions

Since the Faraday screen we observed towards the Taurus–Auriga molecular cloud complex is most likely associated with the molecular gas, we can specify its distance to 140 pc. When spherical symmetry is assumed, the size of the screen is of the order of 2 pc. An intrinsic RM of about $-29\ \mathrm{rad\,m^{-2}}$ requires an excessive value for the thermal electron density or an excessive regular magnetic field component parallel to the line-of-sight, when compared to average Galactic values. The total power maps show no enhanced thermal emission at 1408, 1660, or 1713 MHz towards the Faraday screen which gives an upper limit for the thermal electron density of $n_\mathrm{e} \leq 2\ \mathrm{cm^{-3}}$. In addition, we have checked available Hα data from the *full-sky H-alpha map* constructed by Finkbeiner (2003). No enhanced emission (at the 1σ detection level of 0.52 Rayleigh) related to the molecular gas or the Faraday screens is visible, which constrains n_e to less than $0.8\ \mathrm{cm^{-3}}$ for electrons from hydrogen ionization. With these upper limits for the thermal electron density a regular magnetic field strength exceeding 20 μG along the line-of-sight is needed to explain the intrinsic RM.

Towards the Faraday screen modelled here, the observed rotation measure RM_obs differs from its intrinsic rotation measure RM_int by about $60\ \mathrm{rad\,m^{-2}}$ and the sign of the observed RMs is in opposite direction. In the presence of foreground polarization, which adds to the Faraday rotated background, the observed RM is not a fixed value, but depends on the two frequencies used for its determination and in addition on the amount of foreground polarization adding to the rotated background. This implies no λ^2–dependence of the observed polarization angles in the direction of Faraday screens.

References

Brouw W. N., Spoelstra T. A. Th. (1976) *Astron. Astrophys. Suppl.* **26**, 129.
Dame T. M., Hartmann D., Thaddeus P. (2001) *Astrophys. J.* **547**, 792.
Elias J. H. (1978) *Astrophys. J.* **224**, 857.
Finkbeiner D. P. (2003) *Astrophys. J. Suppl.* **146**, 407.
Goméz G. C., Benjamin R. A., Cox, D. P. (2001) *Astron. J.* **122**, 908.
Reich P., Reich W. (1986) *Astron. Astrophys. Suppl.* **63**, 205.
Reich P., Reich W. (1988) *Astron. Astrophys.* **74**, 7.
Reich W. (1982) *Astron. Astrophys. Suppl.* **48**, 219.
Spoelstra T. T. Th. (1972) *Astron. Astrophys.* **21**, 61.
Taylor J. H., Cordes J. M. (1993) *Astrophys. J.* **411**, 674.
Wolleben M., Reich W. (2004) *Astron. Astrophys.*, submitted.

"The Magnetized Interstellar Medium"
8–12 September 2003, Antalya, Turkey
Eds.: B. Uyanıker, W. Reich & R. Wielebinski

Magnetic Fields and other Parameters of the Diffuse Galactic ISM

Thomas H. Troland

Department of Physics & Astronomy, University of Kentucky, 600 Rose Street, Lexington, KY 40506

Abstract. Observations of magnetic fields in the diffuse ISM of the Galaxy offer important insights into the physics of this gas, and they may provide clues to the processes that transform one phase into another. Here we review the physical nature of the diffuse ISM, concentrating on H I in the CNM and WNM. We also describe the Arecibo Millennium H I absorption survey of Heiles & Troland, highlighting its new observational and data analysis techniques. The results of this survey establish that the median magnetic field strength in the CNM is about 5 μG, very similar to other field strength measurements in less dense and in more dense gas. The absence of any obvious correlation between field strength and gas density for densities $\leq 10^3$ cm^{-3} is now on firm statistical grounds. Understanding this phenomenon presents interesting opportunities for theoretical work. Nonetheless, the magnetic field in the CNM is hardly irrelevant. Its energy is comparable to turbulent energies. Also, the mass-to-flux ratio in this gas is largely subcritical. If this ratio is preserved as the gas becomes self-gravitating, then the magnetic field will be important to subsequent evolution and star formation within the gas.

1 Diffuse gas in the Galaxy

Diffuse gas in the Galaxy is generally considered as the non self-gravitating component of the ISM. Its physical state is controlled by the general galactic radiation and gravitational fields, by the injection of mechanical energy from stellar winds, supernovae and other sources and by the magnetic field. Much of the diffuse ISM is H I. However, H I halos of molecular clouds, with masses comparable to those of the molecular gas, often appear to be gravitationally bound. Whether or not this H I gas is diffuse is a matter of definition.

Diffuse gas exists in a variety of physical states with widely different temperatures and densities. Here we consider primarily the two H I phases, the Cold Neutral Medium (CNM) and the Warm Neutral Medium (WNM). This gas is most easily observed in 21 cm absorption (CNM) and emission (WNM). By mass, H I appears to be about equally divided between these two phases, although the volume filling factor of the WNM is much larger, approximately 50% near the Galactic Plane. Of course, other phases of the diffuse ISM also exist, the Warm Ionized Medium (WIM) and the Hot Ionized Medium (HIM). The WIM is most widely observed in Hα emission (e.g. Haffner et al. 2003). Its temperature, volume density and total mass are probably comparable to those of the WNM. The Hot Interstellar Medium (HIM) is much lower in density and hotter than any other phase. We do not consider this phase any further.

The CNM and WNM have been classically viewed as in pressure equilibrium. Temperatures are maintained by heating from photoejection of electrons from atoms and dust grains. Cooling arises from collisional excitation of various interstellar species, in particular, C^+. A typical value of $P/k \approx 3000$ cm^{-3} K (Jenkins & Tripp 2001, Wolfire et al. 2003). Therefore, if typical temperatures for the CNM and WNM are about 80 K and 8000 K, respectively, then typical densities are about 40 and 0.4 cm^{-3}.

From a theoretical standpoint, two conditions must be satisfied to maintain a thermally stable two-phase ISM. For one, the pressure must lie within a narrow range $P_{\rm min} \leq P \leq P_{\rm max}$. Wolfire et al. (2003) develop an analytic expression for $P_{\rm min}$. They estimate that $P \geq P_{\rm min}$ over most of the galactic disk owing to the weight of the gas in the galactic gravitational field. The second condition for a thermally stable ISM is that $\Gamma \equiv t_{\rm cool}/t_{\rm shk} < 1$ where $t_{\rm cool}$ and $t_{\rm shk}$ are the timescales for gas cooling and shock heating, respectively. If $\Gamma < 1$, then the gas has time to cool between successive shocks and return to thermal equilibrium. Wolfire et al. provide an analytic expression for $t_{\rm cool}$. For the classical WNM, $t_{\rm cool} \approx 6$ Myr while for the classical CNM $t_{\rm cool} \approx 10^4$ yr. The latter timescale is nearly instantaneous, the former is not. Wolfire et al. estimate that $\Gamma < 1$ for the WNM in the galactic disk. Therefore the diffuse ISM should be reasonably well described by the classical two-phase model. However, the value of $t_{\rm shk}$ must vary widely within the disk; it will be smaller near regions of high mass star formation. Therefore, significant portions of the diffuse ISM may not be close to thermal equilibrium in the classical two-phase sense. Also, the condition $P \geq P_{\rm min}$ may not be satisfied at high z where gas pressures decline.

A clearer understanding of the diffuse ISM requires better quality and more statistically complete observational data as well as further theoretical work. Among the observational parameters of interest are temperatures, column densities, turbulent velocity widths and magnetic fields for the CNM and the WNM. From this information, one can infer the spatial distribution and morphology of the diffuse gas, the mass and volume filling factors of its phases, and the distribution of temperatures, Mach numbers and Alfvén Mach numbers and mass-to-flux ratios. This information, in turn, bears upon the astrophysical questions of interest. For example, is the diffuse ISM generally in thermal equilibrium as the classical models suggest or is its state predominantly determined by impulsive shock events? How do various phases of the diffuse ISM interact with each other and transform from one phase to another? How does the diffuse ISM become transformed into self-gravitating gas leading to star formation?

Of special interest to this review are astrophysical questions related to the magnetic field. How important is the field to the energetics of the gas? This question can be answered by comparing magnetic field energy densities to those of the turbulent and thermal motions of the gas. In the strong field case (sub-Alfvénic turbulence), magnetic fields play a significant role in directing gas motions, and the field remains rather uniform. Otherwise, the field plays little role and is very tangled. Another important question is the relationship of magnetic field strength to gas density. If flux freezing is maintained as less dense phases of the diffuse ISM transform into denser phases, then the field strength should increase as a function of density unless gas flows only along the field lines. Therefore, the field strength gas density relationship in the diffuse ISM is an indicator of the process by which low density gas becomes high density gas or else it is an indicator of the efficacy of flux freezing in the diffuse gas. Finally, the mass-to-flux ratio in the densest diffuse gas (CNM) is of considerable interest. This parameter is normally viewed as a measure of the ratio of gravitational to magnetic energy in the ISM. As such, it is rarely considered in studies of non self-gravitating gas. However, the mass-to-flux ratio is conserved in the presence of flux freezing. In such a case, this ratio in the diffuse gas determines the ratio in the self-gravitating gas. And in the self-gravitating gas, this ratio has a fundamental effect upon the nature of star formation.

In this review, we consider the properties of the diffuse ISM in the Galaxy with special emphasis upon (1) measurements of magnetic field strengths and (2) the Millennium Arecibo 21 cm absorption line survey. The Millennium survey has been exhaustively described by Heiles & Troland (2003a,b, 2004a) with further analysis to be presented in subsequent publications. This survey, comprising over 800 hours of telescope time and observations toward 79 extra-galactic continuum sources, represents the largest and most statistically complete study of the CNM and WNM at high latitude (generally, $b > 10°$). The principal motivation for this survey and the need for large amounts of telescope time come from the desire to measure magnetic field strengths via the 21 cm Zeeman effect. However, an important additional outcome from this survey is a wealth of data on other physical parameters of the CNM and WNM. These include temperatures, column densities and turbulent velocity widths.

2 Measuring magnetic field strengths in the diffuse ISM

Several observational techniques exist to measure magnetic field strengths in the diffuse ISM. These have been reviewed numerous times; for example, see Heiles (1996) and Beck (2001). The principal techniques involve (1) galactic synchrotron radiation, (2) the ratio of rotation measures (RM) to dispersion measures (DM) of pulsars and (3) the Zeeman effect in the 21 cm H I line. We disregard here the study of starlight polarization since this technique is sensitive to field *directions* only, not to field strengths.

Each of the techniques for measuring field strengths in the diffuse ISM involves certain assumptions and has various limitations. Moreover, each technique samples different regimes of the gas. For example, the study of galactic synchrotron radiation reveals the volume average field strength subject to several assumptions such as equipartition between magnetic field and cosmic ray energies. In the Solar Neighborhood, such studies suggest $B_{\rm tot} = 6 \pm 1\,\mu$G (Strong et al. 2000). The ratios RM/DM for pulsars reveal the average line-of-sight field component $B_{\rm los}$ and its direction (i.e. towards or away from the observer) along the line-of-sight to the pulsar. In all cases, the measurement of $B_{\rm los}$ applies to the WIM unless an H^+ region lies along the line-of-sight. This technique has yielded estimates of $1.4\,\mu$G for the uniform magnetic field component near the Sun and about $5\,\mu$G for the total field strength. (See review by Heiles 1996.) However, subtle statistical biases in measurements of $B_{\rm los}$ can arise if fluctuations exist in the field strength and electron density along the line-of-sight and if these fluctuations are not statistically independent (Beck et al. 2003). These biases can lead to underestimates or overestimates in $B_{\rm los}$. Finally, the Zeeman effect in the 21 cm H I line reveals the strength and direction of $B_{\rm los}$ in the CNM (H I absorption) and in the WNM (H I emission). Zeeman effect measurements have an important advantage over RM data. They independently sample different velocity components in the H I absorption and emission profiles. Therefore, they can reveal $B_{\rm los}$ in one or more localized regions along the same line-of-sight. However, Zeeman effect measurements are susceptible to a variety of instrumental polarization effects. Also, the effect is usually very weak, requiring very long integration times. Measurements of $B_{\rm los}$ via the H I Zeeman effect typically reveal $|B_{\rm los}| \leq 10\,\mu$G, with many non-detections.

3 The Arecibo Millennium survey

3.1 Introduction

This survey, outlined briefly above, has yielded much information about physical parameters of the CNM and the WNM at high galactic latitudes. In part, the Millennium survey is complementary to recent galactic plane H I absorption studies. These studies make use of either high-resolution galactic plane surveys of emission and absorption (Dickey et al. 2003, Strasser & Taylor 2004) or else VLA observations of H I absorption toward selected extra-galactic continuum sources (Kolpak et al. 2002). Unlike the Millennium survey, the galactic plane studies provide information about diffuse H I gas over a range in $R_{\rm gal}$. However, the Millennium survey is sensitive to all Stokes parameters. As a result, it is sensitive to the Zeeman effect in Stokes parameter V, and it provides crucial estimates of instrumental polarization in Stokes V via data obtained in Stokes Q and U. Details of the Millennium survey have been provided by Heiles & Troland in the publications cited above. Also, Heiles (2004) has reviewed physical properties in the diffuse H I gas, drawing upon many of the results of the Millennium survey.

The purpose of the remainder of this review is twofold. For one, we will review the salient features of the Millennium survey and highlight the new observation and analysis techniques developed for the survey. Also, we will briefly cite key results from the survey regarding both magnetic and non-magnetic properties of the diffuse H I gas.

3.2 Stokes parameter I data analysis

The Millennium survey was designed to study galactic H I emission and absorption along lines of sight toward extra-galactic continuum sources. To keep line profiles as simple as possible, we chose continuum sources at high latitude, generally $|b| > 10°$. All sources used in this survey are listed by Heiles & Troland (2003a). From the magnetic field perspective, this survey differs from earlier studies of the Zeeman effect in H I emission (e.g. Heiles 1989) in that it samples *random* lines of sight through the diffuse gas, not regions with morphologically obvious structures such as H I shells. Arecibo, with its very large collecting area, is the premier instrument for such a study. Although restricted in declination, its point source sensitivity (10 K/Jy) allows for reliable H I absorption observations of relatively weak sources ($S_\nu \approx 2$ Jy). The VLA is capable of observing H I absorption of even weaker sources. However, the VLA provides no information about H I emission. Therefore analysis of H I spin temperatures T_s is impossible, and sensitivity to the Zeeman effect is less owing to the smaller total collecting area.

Single-dish observations of H I absorption and emission toward continuum sources have been carried out for decades (e.g. Hagen, Lilley & McClain 1955). The classic technique is to observe on-source and, also, positions adjacent to the source. The latter observation provides the "expected" emission profile, $T_{\rm exp}(v)$, that is, the best estimate of the emission profile on-source if the source had zero flux. Usually, $T_{\rm exp}(v)$ is taken as the average of four off-source positions equally displaced from the source at position angles of 0, 90, 180 and 270 degrees. The error in $T_{\rm exp}(v)$ is estimated from the maximum differences among the off-source profiles. Finally, the optical depth profile $\tau(v)$ is derived from the difference between the on-source profile and $T_{\rm exp}(v)$, and the spin temperature profile is computed as $T_s(v) = T_{\rm exp}(v)/(1 - e^{-\tau(v)})$.

Several variations on this classic technique were introduced for the Millennium survey. For one, a total of 16 off-source positions were observed for each source. A least-squares fitting process, described by Heiles & Troland (2003a), solves simultaneously for $T_{\rm exp}(v)$ and $\tau(v)$ as well as profiles for all first and second spatial derivatives in the H I emission. This fitting technique yields $T_{\rm exp}(v)$ and $\tau(v)$ corrected for the first and second spatial derivatives. It also yields error profiles for $T_{\rm exp}(v)$ and $\tau(v)$, each representing maximum possible uncertainties owing to third and higher derivatives in the H I emission.

A second variation on the classic H I absorption/emission observations involves Gaussian fitting and a radiative transfer model. This technique is described in detail by Heiles & Troland (2003a) and more succinctly by Heiles (2001). Rather than deriving a $T_s(v)$ profile in the way described above, we fit the profiles $T_{\rm exp}(v)$ and $\tau(v)$ to Gaussians, each of which is assumed to represent a single isothermal component of either CNM or WNM. For each source, we first fit the $\tau(v)$ profile to Gaussians, each representing a CNM component. This fit yields estimates of v_0, τ_0 and Δv for each component, the center velocity, peak optical depth and FWHM, respectively. Next we fit the $T_{\rm exp}(v)$ profile to the sum of two types of Gaussians: (1) Gaussians representing emission from the CNM components previously identified in the $\tau(v)$ profiles, and (2) a very small number of additional Gaussians representing emission from WNM components. In this fit, Gaussians of type 1 are each allowed just one free parameter, the peak emission $T_{0,\rm CMN}$. The fit to $T_{\rm exp}(v)$ yields estimates of T_s and $N(H)$ for each CNM component and estimates of $T_{\rm kmax}$ and $N(H)$ for each WNM component. Values for $T_{\rm kmax}$ are the maximum possible WNM component temperatures defined by their line widths. Knowing T_s and Δv for each CNM component, we can determine the turbulent line broadening $\Delta v_{\rm turb}$. For all fits to $T_{\rm exp}(v)$ and $\tau(v)$, we carefully limited the number of Gaussians such that the fit residuals were not less than the error profiles described above. This technique insures that the number of fitted Gaussian components is never greater than the errors in $T_{\rm exp}(v)$ and $\tau(v)$ warrant. We summarize by listing the quantities derived from our fits to $T_{\rm exp}(v)$ and $\tau(v)$. For each CNM component, we derive T_s, $N(H)$ and $\Delta v_{\rm turb}$. For each WNM component we derive $T_{\rm kmax}$ and $N(H)$.

The fitting process described above includes a radiative transfer model. In particular, we account for the absorption of each CNM component by all those in front of it. Since the order along the line-of-sight of the CNM components is unknown, we permute this order in a series of independent fits. Each permutation results in somewhat different fitted values for T_s and $N(H)$. Also, we assume that a fraction F_k of the WNM lies in front of all CNM components. In principle, F_k can be determined as a fit parameter. In practice, the fits are rather insensitive to F_k. Therefore, we assume possible values of 0, 1/2 and 1 for F_k and make independent fits for each. In light of the radiative transfer model, there are a number of possible fits to $T_{\rm exp}(v)$ and $\tau(v)$ for each source. These fits correspond to different permutations in the order of the CNM components and to the three assumed values of F_k. Each of these fits yields different values for the derived parameters such as T_s. Moreover, uncertainties in the derived parameters are not dominated by errors in the fitting process. Instead, they are dominated by variations in fitted values among the independent fits we perform for each source. Therefore, we have estimated the most probable value of each derived parameter from the ensemble of values for that parameter returned by all of the independent fits. This technique, described by Heiles & Troland (2003a), also returns a formal estimate of the uncertainty in each parameter.

3.3 Results from Stokes parameter I data – non-magnetic parameters

Toward the extra-galactic sources in the Millennium survey, we identified 143 CNM components toward 48 sources and, also, 143 WNM components toward 66 sources. (Some sources, especially those at very high b, had no CNM components.) We present the analysis of these data in great detail in Heiles & Troland (2003b). One important outcome of this analysis is the idea that the CNM exists predominantly in thin sheets. Here we review briefly some of the major conclusions about CNM and WNM in the vicinity of the Sun. Results from the Millennium survey are also reviewed by Heiles (2004).

Temperatures in the diffuse ISM

One important result is that the CNM and the WNM are physically distinct phases of the diffuse ISM, not regions selected observationally by their 21 cm H I absorption or emission. The statistics of T_s for the CNM components and of T_{kmax} for WNM components reveal two distinct populations. The histogram of CNM components peaks near 40 K with some components as low as 15 K and very few above 100 K. In contrast, the histogram of T_{kmax} shows a rather uniform distribution of values out to about 1.5×10^4 K.

The temperature statistics for the CNM and WNM carry some important implications. CNM temperatures as low as 15 K cannot be explained theoretically except in the absence of heating by photoelectric ejection from grains. The implication is that the very coldest CNM components are devoid of grains for unknown reasons. Another important result concerns the distribution of T_{kmax}. Approximately half of the WNM lies at temperatures below 5000 K, that is, significantly cooler than the thermally stable equilibrium value of $\approx$ 8000 K. We conclude, as theoretical studies involving impulsive shock heating have also suggested, that a significant fraction of the WNM is out of thermal equilibrium.

Mass and volume filling fractions of CNM and WNM

From the statistics of $N(H)$ for the CNM and WNM components, we can roughly estimate the division of diffuse H I gas between the two phases and their volume filling factors. Approximately 60% of H I is in the WNM. This mass fraction is much higher than that predicted by classical theories of the ISM (McKee & Ostriker 1978), although it is consistent with the much more recent predictions of Wolfire et al. (2003). Also, we estimate that the WNM has a volume filling factor of very roughly 50% in the galactic plane. Presumably, this fraction increases with distance away from the plane. The CNM, with a typical volume density two orders of magnitude higher than the WNM and similar total mass, occupies a negligible volume.

Turbulence in the CNM

Since our fitting process for CNM components independently determines T_s and the line width, we can estimate Δv_{turb}, as mentioned above. Therefore, we can investigate the range of turbulent Mach numbers M_{turb} in the CNM. We define M_{turb} as the ratio of the one-dimensional turbulent velocity *dispersion* (not FWHM) to the isothermal sound speed. This definition leads to the relation

$$M_{\mathrm{turb}}^2 = 4.2 \left(\frac{\Delta v_{\mathrm{obs}}^2}{\Delta v_{\mathrm{therm}}^2} - 1 \right) \tag{1}$$

where v_{obs} and $\Delta v_{\mathrm{therm}}$ are the observed line width and the thermal contribution to the line width, respectively (see Heiles 2004). Here we have included a correction factor of 3 to convert the measured one-dimensional turbulent line width to three dimensions. Not surprisingly, we find $M_{\mathrm{turb}} >> 1$ for most CNM components. The M_{turb} histogram peaks broadly over the range 2–4 with some values as high as 10. Only a very small fraction of the CNM components have $M_{\mathrm{turb}} < 1$. Clearly, the CNM is highly supersonic as most modern theoretical studies assume.

3.4 Stokes parameter Q, U, V data analysis

All data collected for the Millennium survey were obtained in cross correlation mode with the Arecibo correlator. Heiles et al. (2001) describe this technique which yields simultaneous profiles in all Stokes parameters once appropriate polarization calibration factors have been determined and applied. Heiles & Troland (2004a) describe in detail the analysis of data for Stokes Q, U, and V. Although more complicated, this analysis is similar to that for the Stokes I data described above. That is, we derive through a least-squares fitting process the polarized profiles for the opacity and for the expected emission $T_{\rm exp}(v)_{Q,U,V}$ and $\tau(v)_{Q,U,V}$. From the Stokes V profiles $T_{\rm exp}(v)_V$ and $\tau(v)_V$ we can, at least in principle, derive the Zeeman effect for WNM and CNM components, respectively. In practice, instrumental effects preclude reliable results for the WNM components.

Instrumental polarization – a crucial issue

Since our principal motivation for the Millennium survey was magnetic field studies, we were extremely careful to estimate instrumental polarization effects and correct for them when possible. This effort is crucial because instrumental polarization is often the limiting factor in Zeeman effect observations, especially in the 21 cm H I line. Instrumental polarization can add artifacts to the Stokes V profiles that mimic the Zeeman effect, leading to erroneous measures of the magnetic field. Very briefly, instrumental polarization amounts to any difference in the telescope beam pattern between orthogonal polarizations. That is, instrumental polarization amounts to any non-zero regions in the Stokes parameter Q, U or V telescope beam patterns. For the Zeeman effect, we are principally concerned with the Stokes V beam pattern. However, imperfections in the telescope system lead to coupling among the Stokes parameters, so complete characterization of instrumental polarization relevant to the Zeeman effect requires data for all Stokes parameters.

Instrumental polarization in (e.g.) the Stokes V beam pattern can be described in terms of a series of Fourier components in position angle about beam center. The first component amounts to a two-lobed pattern with peaks of opposite sign on either side of beam center. This type of instrumental polarization is called *beam squint* since it is equivalent to a slight offset in position on the sky between the right and left circular polarization telescope beams. The second Fourier component amounts to a four-lobed "cloverleaf" pattern with peaks of the same sign on opposite sides of beam center. This type of instrumental polarization is called *beam squash.* Ideally, beam squint is expected for the Stokes V beam pattern, and beam squash is expected for Stokes Q and U patterns. However, the Arecibo telescope exhibits both instrumental effects in all polarized Stokes parameters.

We developed a least-squares fitting process to account for beam squint and beam squash in the Stokes V profiles. This process is based upon the expectation that the Stokes V telescope pattern is fixed with respect to the telescope feed system; hence, the pattern rotates on the sky as the telescope tracks a source. If so, instrumental polarization effects in $T_{\rm exp}(v)_V$ and $\tau(v)_V$ will vary as $\cos(PA)$ and $\cos(2PA)$ for beam squint and squash, respectively, where PA is the parallactic angle of the source. Our least-squares fitting process for $T_{\rm exp}(v)_V$ and $\tau(v)_V$ includes terms in $\cos(PA)$ and $\cos(2PA)$. Therefore, it removes these effects from the Stokes V profiles.

This technique assumes that the polarized beam pattern of the telescope remains fixed relative to the telescope feed system. This assumption need not be entirely correct. As a further estimate of instrumental effects, we make use of the linear polarization profiles $T_{\rm exp}(v)_{Q,U}$ and $\tau(v)_{Q,U}$ for each source. Arecibo beam squint and beam squash are known to be about 10 times higher in linear than in circular polarization. At the same time, the H I line is not expected to exhibit intrinsic linear polarization. So any apparent polarization in $T_{\rm exp}(v)_{Q,U}$ and $\tau(v)_{Q,U}$ is instrumental. Therefore, we multiply by 0.1 the $T_{\rm exp}(v)_{Q,U}$ and $\tau(v)_{Q,U}$ profiles for each source. These scaled down profiles are an estimate of the maximum likely instrumental effects in $T_{\rm exp}(v)_V$ and $\tau(v)_V$. To derive the Zeeman effect reliably from $T_{\rm exp}(v)_V$ and $\tau(v)_V$, the presumed Zeeman signature in the Stokes V profiles must (1) have beam squint and beam squash effects removed as described above and (2) be significantly larger in amplitude than 0.1 times the Stokes Q and U profiles.

Careful consideration of instrumental effects, as outlined above, has yielded two general conclusions. For one, we cannot reliably derive the Zeeman effect from $T_{\rm exp}(v)_V$. That is, we cannot derive magnetic field strengths from the Arecibo data for the WNM. However, we can usually do so from the $\tau(v)_V$ profiles, leading to magnetic field measurements for the CNM. The fundamental reason for this difference lies in the nature of the expected profiles compared to the opacity profiles. The latter are derived, in effect, from the difference between on-source and off-source observations. Therefore, instrumental effects subtract out to first order, and the $\tau(v)_V$ profiles can provide reliable estimates of the CNM magnetic field.

3.5 Results from Stokes V data – the CNM magnetic field

Heiles & Troland (2004a) present magnetic field results for 136 CNM components seen against 41 sources. The majority of these results are non-detections (only 22 results are detections at the 2.5 σ level or higher). However, the magnetic field sensitivity is high, and the sampling of local CNM is random. Therefore, this sample represents a statistically significant one for investigating the CMN magnetic field. In a subsequent publication (Heiles & Troland 2004b) we will present a complete statistical analysis of these results and their significance to the diffuse ISM. Here we summarize the results of some of this analysis.

Magnetic field strengths in the CNM

The magnetic field in the CMN is weak. Heiles & Troland (2004b) carefully analyze the statistics of the measured line-of-sight field strengths and other parameters derived for the CNM from the Millennium survey. This sample includes 69 CMN components with magnetic field detections or meaningful upper limits. Heiles & Troland consider the relationship between the probability distribution function (pdf) of the observed $B_{\rm los}$ and that of the total field strength $B_{\rm tot}$. From this analysis, they find that the median CNM magnetic field strength is relatively well defined, $B_{\rm tot} \approx 5.4\,\mu$G. This value is nearly identical to the local volume average magnetic field derived from galactic synchrotron data ($B_{\rm tot} = 6 \pm 1\,\mu$G). Also, it is nearly identical to the total field strength derived for the WIM from pulsar RM and DM data ($B_{\rm tot} \approx 5\,\mu$G). Yet the CNM volume density is likely to be two orders of magnitude higher than the average density of the diffuse ISM which, in turn, is comparable to the average density of the WIM. In the diffuse ISM, there is no indication whatever of a connection between gas density and field strength over two orders of magnitude in density. Previous studies have described this lack of connection (see the review by Crutcher, Heiles & Troland 2003). However, the most recent analysis of Millennium survey data provides the best statistical evidence by far of this theoretically unexpected behavior.

Evidently, conventional concepts of flux freezing do not apply in the diffuse ISM, or else CNM forms out of lower density gas by motions almost entirely along the field. Yet no obvious mechanism exists to drive this motion, especially on the relatively small scales that characterize concentrations of CNM. Also, the field would need to be relatively strong to collimate such flows. Zweibel (2002) has considered the effect of turbulence upon ambipolar drift. She estimates that this process is much faster in a turbulent medium. Perhaps flux freezing does not apply so rigorously in the turbulent diffuse ISM as conventional thought suggests. Alternately, other processes may be at work to weaken the field as diffuse gas becomes denser. One possibility is the annihilation of oppositely-directed fields in adjacent concentrations of gas. It is fair to say that the magneto-physics of the diffuse ISM is still very poorly understood.

Magnetic energy densities and mass-to-flux ratios in the CNM

Apart from the field strength-volume density relationship, other important results about CNM magnetic fields come from the Millennium survey. First is the ratio of magnetic to turbulent pressures $\beta_{\rm turb}$, where $\beta_{\rm turb}$ is defined analogously to the more conventional ratio $\beta_{\rm th}$ of thermal to magnetic pressures. We define $\beta_{\rm turb}$ in the relation

$$\beta_{\rm turb} = \frac{P_{\rm turb}}{P_{\rm mag}} = \frac{2\sigma(v)^2_{\rm turb,1D}}{v_A^2} \tag{2}$$

where $\sigma(v)_{\rm turb}$ is the one-dimensional velocity /em dispersion (not the FWHM) associated with turbulent motions and v_A is the Alfvén velocity. Estimates of v_A require the volume density. For CNM components identified in the Millennium survey, densities can be estimated from T_s by assuming a constant interstellar $P/k = 3000$ cm^{-3} K. For a typical $T_s = 50$ K, $B_{\rm tot} = 5.4\,\mu$G and $\sigma(v)_{\rm turb} = 1$ km s^{-1}, $\beta_{\rm turb} \approx 1$. That is, magnetic and turbulent pressures are quite comparable on the average. Equivalently, magnetic and turbulent energies are in approximate equipartition. Crutcher (1999) considered Zeeman effect and other data for much denser self-gravitating clouds. Data for these regions also suggest magnetic equipartition. However, a striking exception to magnetic equipartition appears to exist in the "veil" of neutral material lying in front of the Orion Nebula. In this region, field strengths are high ($B_{\rm los} \geq 50\,\mu$G) as revealed by aperture synthesis Zeeman effect studies of H I absorption lines against the nebula (Troland et al. 2004). Abel et al. (2004) perform model calculations suggesting that volume densities are relatively low in the veil ($\approx 10^3$ cm^{-3}). Under these conditions, the magnetic pressure is considerably greater than the turbulent pressure, at least in the narrowest H I component ($\Delta v_{\rm obs} = 2$ km s^{-1}). By some standards, the Orion veil can be considered diffuse CNM. However, its origin is almost certainly associated with the star-forming OMC-1 cloud. Therefore, its history is likely to be quite different from the history of more typical CNM in the Galaxy.

Finally, magnetic field strengths from the Millennium survey permit an estimate to be made of the mass-to-flux ratio in the CNM. In self-gravitating clouds, there is a critical mass-to flux ratio. If the actual ratio is less than the critical value, then magnetic forces dominate gravitational forces, and the cloud cannot collapse in the presence of flux freezing. Such a cloud is said to be magnetically *subcritical*. The actual mass-to-flux ratio divided by the critical mass-to-flux ratio is often defined as λ. In observational units, $\lambda \approx 0.5 \times 10^{-20}\ N(\mathrm{H\,I})/B$, with $N(\mathrm{H\,I})$ in cm^{-3} and B in μG. Heiles & Troland find $N(\mathrm{H\,I}) \leq 3 \times 10^{20}$ cm^{-3} for most sheets of CNM, where statistical corrections have been applied to convert the pdf of observed $N(H)$ into the pdf of $N(H)$ perpendicular to the sheets. Therefore, $\lambda < 0.25$ for the median value $B_{\rm tot} \approx 5.4\,\mu$G. Evidently, the CNM is often magnetically subcritical. If λ is conserved during the process by which CNM becomes self-gravitating gas, then this gas, too, will be magnetically subcritical and incapable of gravitational collapse as long as flux freezing persists.

4 Other measures of magnetic fields in diffuse H I gas

The 21 cm Zeeman effect has been used extensively to measure magnetic fields in H I emission lines. These observations have been done principally by Heiles at the Hat Creek Observatory, and they are reviewed briefly by him (Heiles 2004). The H I emission line Zeeman data sample magnetic fields toward morphologically obvious H I emission features. Therefore, they are statistically different from the observations of the Millennium survey that sample random lines-of-sight. Examples of morphologically obvious features studied for the H I Zeeman effect include H I shells and supershells (Heiles 1989), dark clouds (Heiles 1988, Goodman & Heiles 1994) and the H I emission in the Orion region (Heiles 1997). These data reveal that $B_{\rm los} \approx 5$–$10\,\mu$G, with many non-detections.

The ensemble of H I emission line data is consistent with $B_{\rm tot} \approx 10\,\mu$G. This value is only marginally higher than the estimated $B_{\rm tot} \approx 5.4\,\mu$G in the CNM. However, physically meaningful comparisons between these two field strength estimates are complicated by two factors. For one, H I emission samples lower density gas on the average than H I absorption. Second, morphologically obvious features may have stronger fields as a result of their histories. For example, the fields in H I shells and supershells have presumably been amplified by shock processes. And H I associated with the Orion region or with dark clouds is likely to be self-gravitating. Gas densities and field strengths in these regions may have been enhanced by gravitational compression.

It is interesting to note that field strengths measured in dark clouds via the 18 cm OH Zeeman effect rarely show $B_{\rm los} > 20\,\mu$G with many limits $\leq 10\,\mu$G (e.g. Crutcher 1999). Densities in these regions are likely $\geq 10^3$ cm^{-3}, another order of magnitude higher than in the CNM and still without any significant increase in field strength. Taken as a whole, magnetic field data sampling density regimes from 0.1 cm^{-3} (pulsar data for the WIM) to 10^3 cm^{-3} (OH Zeeman effect) reveal no more than a factor of two increase in apparent field strength. If $B \propto n^\kappa$, then $\kappa \leq 0.1$. In denser self-gravitating gas ($n \geq 10^3$ cm^{-3}), gas densities and field strengths are correlated with $\kappa \approx 0.5$. These results and their implications are reviewed in this volume by Crutcher.

5 Conclusions

It is well known that observational studies of interstellar magnetic fields are maddeningly difficult. Each available technique has serious drawbacks and samples different components of the field in different interstellar regimes. Moreover, virtually every technique involves measurement of polarization. Polarization measurements, especially measurements of very small fractional polarizations (e.g the Zeeman effect) are subject to serious instrumental effects. Nonetheless, a very significant body of observational data now exists regarding magnetic fields in the ISM. In the context of this review, it is field *strength* data that are of interest.

The absence of any significant observed connection between B and n in the low density gas is not news. This curious result was noted by Troland & Heiles (1986). However, more recent Zeeman effect results place the conclusion on a much firmer statistical basis. It is now much more difficult to argue that the apparent insensitivity of B to n is an effect of limited sampling. Disappointing as this phenomenon may be to observers, it is real, and it begs for a clearer theoretical explanation. At the same time, the magnetic field has hardly been found to be irrelevant in the diffuse ISM or elsewhere. In the CNM, its energy density is comparable to that of turbulent motions. Therefore, the field must play a significant role in CNM gas dynamics. And the CNM mass-to-flux ratio appears to be subcritical. If this ratio is conserved in the transformation to self-gravitating gas, then the field will play an important role in the subsequent evolution of this gas toward star formation. Of course, the processes whereby lower density gas is transformed into higher density gas, and the role of the magnetic field in these processes, are still quite mysterious. Further observational studies of magnetic field strengths and additional theoretical work will be necessary to clarify these issues.

Acknowledgements

It is a pleasure to acknowledge my many fruitful collaborations with two other well-known magnetic field aficionados, Carl Heiles and Richard Crutcher. These collaborations now span several decades. The Arecibo Millennium survey is the brainchild of Heiles, and I have learned much from my association with this exhaustive project. The success of this project is testimony to the importance of careful attention to observational detail and ample supplies of Barrilito 3-star rum. I am very grateful to Crutcher for his assistance in formatting this manuscript, and I thank the organizers of the Antalya conference for their extraordinary efforts. This work was partially supported by NSF grants AST-9988341 and AST-0307642.

References

Abel, N. P., Brogan, C. L., Ferland, G. J., O'Dell, C. R. & Troland, T. H. (2004) *Astrophys. J.*, submitted for publication.
Beck, R. (2001) *Space Sciences Rev.* **99**, 243.
Beck, R., Shukurov, A., Sokoloff, D. & Wielebinski, R. (2003) *Astron. Astrophys.* **411**, 99.
Crutcher, R. M. (1999) *Astrophys. J.* **520**, 706.
Crutcher, R. M., Heiles, C. & Troland, T. H. (2003) in *Turbulence and Magnetic Fields in Astrophysics*, eds. E. Falgarone, T. Passot, Springer, p. 155.
Dickey. J. M., McClure-Griffiths, N. M., Gaensler, B. M. & Green, A. J. (2003) *Astrophys. J.* **585**, 801.
Goodman, A. A. & Heiles, C. (1994) *Astrophys. J.* **424**, 208.
Haffner, L. M., Reynolds, R. J., Tufte, S. L., Madsen, G. L., Jaehnig, K. P. & Percival, J. W. (2003) *Astrophys. J.* **149**, 405.
Hagen, J. P., Lilley, A. E. & McClain, E. F. (1955) *Astrophys. J.* **122**, 361.
Heiles, C. (1988) *Astrophys. J.* **324**, 321.
Heiles, C. (1989) *Astrophys. J.* **336**, 808.
Heiles, C. (1996) in *Polarimetry of the Intersteller Medium*, eds. W. G. Roberge, D. C. B. Whittett, ASP Conf. Ser. **97**, p. 457.
Heiles, C. (1997) *Astrophys. J. Suppl.* **111**, 245.
Heiles, C. (2001) *Astrophys. J.* **551**, L105

Heiles, C. (2004) in *Milky Way Surveys: The Structure and Evolution of Our Galaxy*, 5th Boston University Astrophysics Conference, eds. D. Clemens, T. Brainerd, R. Shah, ASP Conf. Ser., in press.
Heiles, C., Perillat, P., Nolan, M., Lorimer, D., Bhat, R., Gosh, T., Howell, E., Lewis, M., O'Neil, K., Salter, C. & Stanimirovic, S. (2001) *Publ. Astron. Soc. Jap.* **113**, 1247.
Heiles, C. & Troland, T. H. (2003a) *Astrophys. J. Suppl.* **145**, 329.
Heiles, C. & Troland, T. H. (2000b) *Astrophys. J.* **586**, 1067.
Heiles, C. & Troland, T. H. (2004a) *Astrophys. J.*, accepted for publication.
Heiles. C. & Troland, T. H. (2004b) *Astrophys. J.*, in preparation.
Jenkins, E. B. & Tripp, T. M. (2001) *Astrophys. J. Suppl.* **137**, 297.
Kolpak, M. A., Jackson, J. M., Bania, T. M. & Dickey, J. M. (2002) *Astrophys. J.* **578**, 868.
McKee, C. F. & Ostriker, J. P. (1978) *Astrophys. J.* **218**, 148.
Strasser, S. & Taylor, A. R. (2000) *Astrophys. J.*, accepted for publication.
Strong, A. W., Moskalenko, I. V. & Reimer, O. (2000) *Astrophys. J.* **537**, 763.
Troland, T. H., Crutcher, R. M., Roberts, D. A., & Goss, W.M. (2004) *Astrophys. J.*, in preparation.
Troland, T. H. & Heiles, C. (1986) *Astrophys. J.* **301**, 339.
Wolfire, M. G., McKee, C. F., Hollenbach, D. & Teilens, A. G. G. M. (2003) *Astrophys. J.* **587**, 278.
Zweibel, E. G. (2002) *Astrophys. J.* **567**, 962.

"The Magnetized Interstellar Medium"
8–12 September 2003, Antalya, Turkey
Eds.: B. Uyanıker, W. Reich & R. Wielebinski

Heating of the ISM by Alfvén-wave Damping

Felix Spanier

Institut für Theoretische Physik IV, Ruhr-Universität Bochum, Universitätsstr. 150, 44801 Bochum

Abstract. We calculate the heating rate from damping of Alfvén waves in the warm ionized medium. An anisotropic power spectrum for magnetic fluctuations was used, which had been derived from electron fluctuations by kinetic calculations. Several damping processes were considered: collision Landau damping, Joule heating, viscous damping and ion-neutral collisions.

1 ISM Scenario

We consider a scenario found in the **Warm Intercloud Medium** with the following parameters: temperature $T \approx 10^4$ K, particle density $n \approx 0.2$ cm^{-3} and a background magnetic field $B = 4\,\mu$G. Under these conditions we find an efficient cooling mechanism with the cooling rate

$$L_R = 5 \cdot 10^{-24}\, n_e^2 \text{ erg s}^{-1} \text{ cm}^{-3} \tag{1}$$

as proposed by Minter & Spangler (1997).

As source of fluctuations in the ISM one finds a mixture of Alfvén and fast magnetosonic waves. For our calculation of the heating rate, we will **focus on Alfvén Waves**. As Spangler (1991) points out these waves must have wave numbers in the regime

$$k_{\text{min}} = \frac{2\pi}{10^{17}\text{cm}}\ ,\ k_{\text{max}} = \frac{2\pi}{10^{7}\text{cm}}$$

which is given by the ion inertia length on the one hand and on the distance between two clouds on the other hand.

2 Wave Spectrum

We use an anisotropic power spectrum of electron density fluctuations from Spangler (1991)

$$P_{nn} = \frac{C_N^2}{(k_\parallel^2 + \Lambda k_\perp^2)^{\frac{2+s}{2}}} \tag{2}$$

To derive the magnetic fluctuation spectra a kinetic approach is needed (Schlickeiser & Lerche 2002)

$$\frac{P_{\text{yy}}^{\text{A}}(\vec{k})}{B_0^2} = \frac{\Omega_{\text{p}}^2 \sin^2\theta}{9V_{\text{A}}^2 k^2}\frac{P_{\text{nn}}^{\text{A}}(\vec{k})}{n_{\text{e}}^2} \tag{3}$$

whereas for fast magnetosonic waves the relation between both spectra is nearly linear.

The constant C_N is defined by normalisation over the total fluctuating power

$$\int d^3k\, P_{nn}(\vec{k}) \quad = \quad (\delta n_e)^2 \tag{4}$$

As the power is splitted into two parts for magnetosonic and Alfvén waves, we introduce two constants, C_A and C_M which determine the magnetic fluctuations.

$$(\delta B_A)^2 \quad = \quad \int d^3k P_{yy}^A(\vec{k}) \tag{5}$$

3 Damping Processes

For a given damping rate the energy dissipation rate is given by:

$$\epsilon_i = \int d^3 k P^A_{yy} 2\gamma_i \tag{6}$$

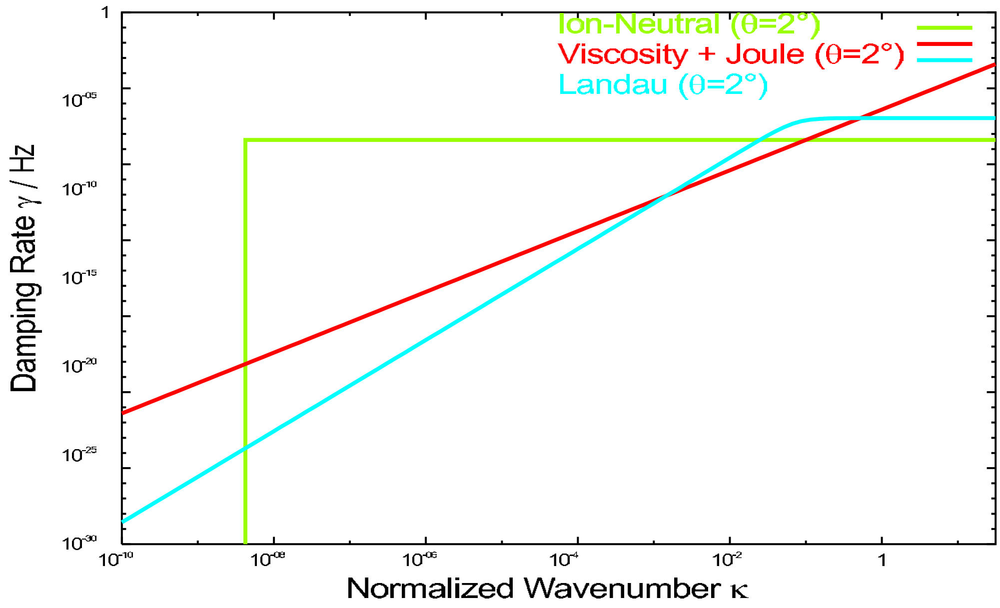

Fig. 1. Damping rates at $\theta = 2°$

Four different processes have been included in the calculation:

- Collisionless Landau damping
- Viscous damping
- Joule heating
- Ion-Neutral collisions

3.1 Joule Heating

Joule heating is related to the resistivity of the plasma and the currents. We take the formula from Braginskii (1965)

$$\sigma_\perp = \frac{\omega_{pe}^2}{4\pi\nu_e}, \sigma_\parallel = 1.96\sigma_\perp \tag{7}$$

resulting in

$$\gamma_J(k) = \frac{\nu_e c^2 k^2}{2\omega_{pe}^2}\left(\cos^2\theta + 0.51\sin^2\theta\right) \tag{8}$$

Joule heating is **neglected in favor of viscosity**.

3.2 Viscosity

Viscosity was proposed by Hollweg (1985), the parameter η_0 cancels out due to the incompressibility of Alfvén waves

$$\gamma_V(k) = \frac{k^2}{2m_p n_e}\left((\eta_1^p + \eta_1^e)\sin^2\theta + (\eta_2^p + \eta_2^e)\cos^2\theta\right) \tag{9}$$

The electron contribution is small compared to the proton contribution

$$\gamma_V(k) \simeq 0.15\frac{k_B T_p}{m_p c^2}\frac{k^2 c^2 \tau_i}{(\Omega_p \tau_i)^2}\left(\sin^2\theta + 4\cos^2\theta\right) \tag{10}$$

Introducing

$$k_c = \frac{\Omega_p}{V_A}\ ,\ \kappa = \frac{k}{k_c}$$

we find for Joule and viscous damping together

$$\gamma_{V+J} = 10^{-7}\kappa^2\left(\sin^2\theta + 4\cos^2\theta\right) \tag{11}$$

As Joule and viscous damping have the same k^2 dependence and similar angular dependence we may sum them up. Integrating with (6) gives

$$\epsilon_{V+J} = 4\cdot 10^7 \frac{1+s}{3-s}(\delta B_A)^2 k_c^2 \frac{\kappa_{\mathrm{max}}^{3-s} - \kappa_{\mathrm{min}}^{3-s}}{\kappa_{\mathrm{max}}^{1+s} - \kappa_{\mathrm{min}}^{1+s}} H_{V+J}(\Lambda, s) \tag{12}$$

$$H_{V+J}(\Lambda,s) = \frac{3F\left(\frac{2+s}{2},1;3;1-\Lambda^{-1}\right)}{8F\left(\frac{2+s}{2},\frac{1}{2};\frac{5}{2};1-\Lambda^{-1}\right)} + \frac{3F\left(\frac{2+s}{2},2;4;1-\Lambda^{-1}\right)}{8F\left(\frac{2+s}{2},\frac{1}{2};\frac{5}{2};1-\Lambda^{-1}\right)} \tag{13}$$

resulting in

$$\epsilon_{V+J} = 10^{-39}\mathrm{erg\ s^{-1}cm^{-3}}(\Lambda = 1) \tag{14}$$

This gives only a small contribution, so it has **no influence on ISM heating**.

3.3 Collisionless Landau Damping

We are using the damping rate for obliquely propagating shear Alfvén waves (Ginzburg 1961, p.218, Eq. (14.56))

$$\begin{aligned}\gamma_L &= \left(\frac{\pi}{8}\right)^{1/2}\frac{\omega^3}{\Omega_\mathrm{p}^2}\frac{v_\mathrm{e}}{V_\mathrm{A}}\frac{\tan^2\theta}{\sin^2\theta + 3(\omega^2/\Omega_\mathrm{p}^2)\cos^2\theta} \\ &\quad \times\left(v_\mathrm{i}^2/v_\mathrm{e}^2 + (\sin^2\theta + 4\cos^2\theta)\exp[-V_\mathrm{A}^2/(2v_\mathrm{i}^2\cos^2\theta)]\right) \\ &\simeq \left(\frac{\pi}{8}\right)^{\frac{1}{2}}\frac{m_e}{m_p}v_e k_c \kappa^3 \frac{\cos\theta + \sin^2\theta}{\sin^2\theta + 3\kappa^2\cos^4\theta}\end{aligned} \tag{15}$$

Inserting into Eq. (6) yields

$$\epsilon_L = 1.1\cdot 10^{-5}\frac{1+s}{2-s}v_e k_c (\delta B_A)^2 \frac{\kappa_{\mathrm{max}}^{2-s} - \kappa_{\mathrm{min}}^{2-s}}{\kappa_{\mathrm{max}}^{1+s} - \kappa_{\mathrm{min}}^{1+s}} H_L(\Lambda, s) \tag{16}$$

$$H_L(\Lambda,s) = \frac{3F\left(\frac{2+s}{2},1;3;1-\Lambda^{-1}\right)}{8F\left(\frac{2+s}{2},\frac{1}{2};\frac{5}{2};1-\Lambda^{-1}\right)} \tag{17}$$

Approximations

$$H_L(\Lambda \gg 1) \simeq const \tag{18}$$

$$H_L(\Lambda \ll 1) \propto \Lambda^{1/2} \tag{19}$$

For given ISM parameters we find

$$\epsilon_L \simeq 3.8\cdot 10^{-42}\mathrm{erg\ s^{-1}cm^{-3}}(\Lambda = 1) \tag{20}$$

Collisionless Landau damping can be ignored for any value of Λ.

Comparison to Fast Magnetosonic Waves

Lerche & Schlickeiser (2001):

$$\begin{aligned} R(\Lambda=1) &= \frac{\epsilon_L^A(\Lambda=1)}{\epsilon_L^M(\Lambda=1)} \simeq 10^{-20}\frac{(\delta B_A)^2}{(\delta B_M)^2} && (21)\\ R(\Lambda\gg 1) &\simeq 10^{-20}\Lambda^{s/2}\frac{(\delta B_A)^2}{(\delta B_M)^2} && (22)\\ R(\Lambda\ll 1) &\simeq 10^{-20}\Lambda^{-s/2}\frac{(\delta B_A)^2}{(\delta B_M)^2} && (23) \end{aligned}$$

3.4 Ion-Neutral Damping

$$\begin{aligned} \gamma_{\mathrm{N}}(k) &\simeq \nu_{\mathrm{N}}\cos^2\theta\ ,\ \kappa \geq \kappa_{\mathrm{N}}\cos\theta && (24)\\ \nu_{\mathrm{N}} &= 4\cdot 10^{-9} n_{\mathrm{H}}\ \mathrm{Hz} && (25)\\ \kappa_{\mathrm{N}} &= \frac{\nu_N\ [\mathrm{Hz}]}{B[\mathrm{G}]} && (26) \end{aligned}$$

γ_N holds for propagation angles $\mid\theta\mid\leq\frac{\pi}{2}-\omega_{\mathrm{R}}/43\Omega_{\mathrm{p}}$
Integrating considering the critical wave number

$$\begin{aligned} \epsilon_N &= \frac{2}{\pi(2-s)(4-s)}\nu_N t_E^{\frac{s+1}{2}}(\delta B_A)^2 H_N(\Lambda,s) && (27)\\ H_N(\Lambda,s) &= \frac{3F(\frac{2+s}{2},2;3-\frac{s}{2};1-\Lambda)}{4F(\frac{2+s}{2},\frac{1}{2};\frac{5}{2};1-\Lambda)} && (28)\\ \epsilon_N &= 1.74\cdot 10^{-29}\mathrm{erg\ s^{-1}cm^{-3}} && (29) \end{aligned}$$

We have two approximations for H_N:

$$\begin{aligned} H_N(\Lambda\gg 1) &\simeq 2^{s-3}(4-s)(2-s) && (30)\\ H_N(t_E<\Lambda\ll 1) &\simeq \frac{s+1}{(4-s)(2-s)^2}\Lambda^{-s/2} && (31) \end{aligned}$$

This is the **most important process**, though the heating rate is still too small to maintain the temperature balance.

4 Conclusions

- Ion-Neutral Damping is the dominant damping process in Alfvén waves
- Anisotropy can reduce damping for perpendicular waves
- Alfvén waves **cannot contribute significantly to the temperature balance of the ISM**

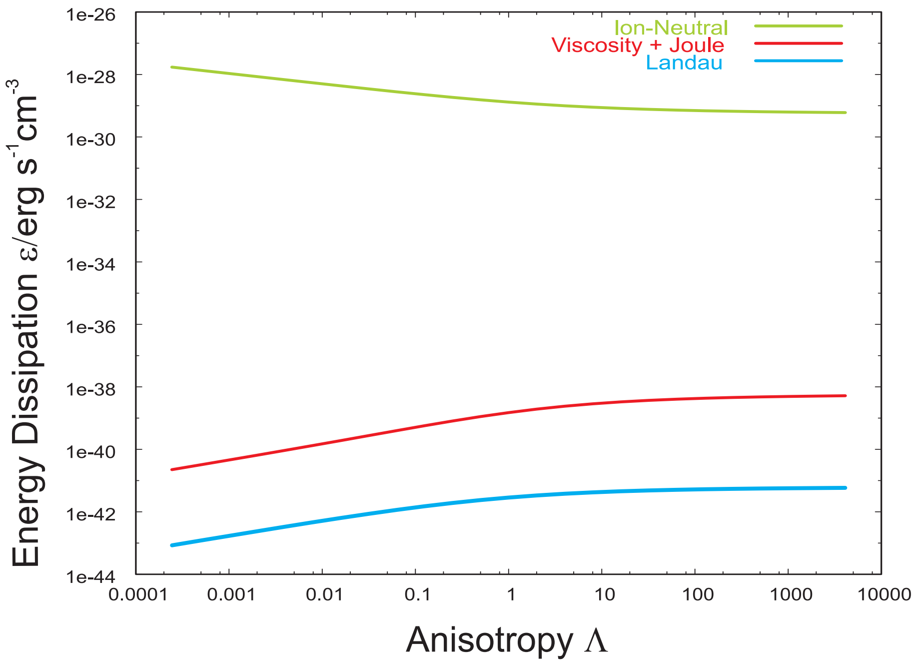

Fig. 2. Energy dissipation rate vs. anisotropy parameter Λ

References

Braginskii, S. I. (1965) *Rev. Plasma Phys.* **1**, 205
Ginzburg, V. I. (1961) *Propagation of Electromagnetic Waves in Plasma*, Pergamon Press, New York
Hollweg, J. V. (1985) *J. Geophys. Res.* **90**, 7620
Kulsrud, R. M., & Pearce, W. P. (1969) *Astrophys. J.* **156**, 445
Lerche, I., & Schlickeiser, R. (1982) *Mon. Not. R. Astron. Soc.* **201**, 1041
Lerche, I., & Schlickeiser, R. (2001) *Astron. Astrophys.* **366**, 1008 (paper I)
Lerche, I., & Schlickeiser, R. (2002) *Astron. Astrophys.* **383**, 319
Minter, A. H., & Spangler, S. R. (1997) *Astrophys. J.* **485**, 182
Schlickeiser, R., & Lerche, I. (2002) *J. Plasma Phys.***68**, 191
Spangler, S. R. (1991) *Astrophys. J.* **376**, 540